A Sulfur Cathode Design Strategy for Polysulfide Restrictions and Kinetic Enhancements in Li-S Batteries through Oxidative Chemical Vapor Deposition

Yuxuan Zhang<sup>1</sup>, Han Wook Song<sup>2</sup>, Kyle R. Crompton<sup>3</sup>, Xixian Yang<sup>4</sup>, Kejie Zhao<sup>4</sup>, Sunghwan Lee<sup>1</sup>\*

- 1. School of Engineering Technology, Purdue University, West Lafayette, IN 47907, United States
- 2. Center for Mass and Related Quantities, Korea Research Institute of Standard and Science, Daejeon 34113, South Korea
- 3. Power and Energy Systems Division, Naval Surface Warfare Center Crane Division, Crane, IN 47522, United States
- 4. School of Mechanical Engineering, Purdue University, West Lafayette, IN 47907, United States

**Keywords:** lithium-sulfur battery, cathode, polysulfide shuttling, oxidative chemical vapor deposition, PEDOT

#### **Abstract**

Lithium-sulfur (Li-S) batteries offer a promising solution for achieving high-density and low-cost energy storage devices. However, the practical utilization of Li-S batteries is hindered by the main bottleneck of polysulfides transport from the cathode to the electrolyte and anode, which leads to the detrimental degradation of the electrolyte and non-uniform microstructure evolution on the anode, ultimately resulting in rapid capacity fading. To overcome this limitation, we propose a groundbreaking mitigation strategy that leverages the oxidative chemical vapor deposition (oCVD) technique to limit the shuttling of polysulfides in the cathode. This gas-phase approach is unique in that highly conducting and conformal polymer coating entirely eliminates the use of traditional binders in the cathode while enhancing the kinetic conditions of the sulfur conversion and inhibiting the shuttling of polysulfides during battery operation. Complementary experimental and theoretical investigations identify that polysulfides are physically and chemically confined in the cathode region. The sulfur cathode manufactured using this approach demonstrates high active material loading (90 wt.%), a high sulfur utilization ratio of 84.4% (~1,413 mAh g<sup>-1</sup> at 0.1 C), and capacity retention of 85% after 300 cycles (~810 mAh g<sup>-1</sup>) at 0.5 C. The pouch cell also showcases a high specific energy of up to 202 Wh kg<sup>-1</sup> with a low electrolyte/sulfur ratio of 4.55, proving the immense potential for practical applications.

#### 1. Introduction

Lithium-sulfur (Li-S) batteries have emerged as one the most promising next-generation energy storage technologies for potential applications in electric vehicles, portable electronics, and smart grids due to their high theoretical energy density (2600 Wh kg<sup>-1</sup>) and low price.<sup>1,2</sup>

However, further advancement and adoption of Li-S batteries have been hindered due to still remaining critical challenges in the sulfur cathode.<sup>3,4</sup> For the cathode active materials, the low intrinsic conductivity of the sulfur cathode results in low utilization of sulfur since the insufficient electron transport.<sup>4,5</sup> It has been also reported that the large volume variation (~78%) of the sulfur cathode and its resulting electrode degradation is the main origin of rapid capacity fading.<sup>6</sup> Especially the soluble intermediate polysulfides (Li<sub>2</sub>S<sub>n</sub>, 4≤n≤8) generated during the discharge-charge process, which can freely migrate between the cathode and anode (known as the shuttle effect), leading to the cathode capacity degradation and Li metal anode fading.<sup>7,9</sup> For binder materials, traditional polyvinylidene difluoride (PVDF) has been used due to its adhesion capability and electrochemical thermal stability for battery applications.<sup>10-12</sup> However, PVDF forms highly resistive interfaces with sulfur and conductive additives because of its electronically non-conducting nature. In addition, due to the nonfunctionalized chain structure, PVDF is unable to restrict the transport of polysulfides between the electrodes.<sup>12, 13</sup> The use of PVDF should be further limited owing to its strong chemical interaction with Li<sub>2</sub>S as reduces the efficient utilization of active materials while increasing the polarization of the cathode.<sup>14</sup>

Several strategies were suggested to mitigate the issues in the sulfur cathode.<sup>6, 15</sup> Carbonaceous materials with mechanical flexibility (e.g., carbon spheres) were employed as sulfur hosts to accommodate the large volume change of the sulfur cathode.<sup>16-18</sup> Due to the higher conductivity of carbon-based materials, these carbonaceous materials also enhanced the overall conductivity of the cathode.<sup>19, 20</sup> Yet the weak interactions with non-polar carbon in the carbonaceous materials and polar polysulfides may not effectively restrict the

problematic polysulfides shuttling. <sup>21, 22</sup> Metal compounds such as oxides, carbides, phosphides, and nitrides have been also employed to mitigate polysulfide shuttling by physical and chemical entrapment.<sup>23-27</sup> However, this approach may take more than 30 wt. % of the sulfur cathode to restrict the shuttle effect. Furthermore, additional conducting additives (carbon-based or conductive polymers) need to be coupled due to the low conductivity of these metal compounds. Such a large amount of inactive materials (i.e., metal compounds and conductive additives) will inevitably decrease the energy density of a battery.<sup>28, 29</sup> Conducting polymers such as polypyrrole, polyethylene oxide, and poly (3, 4-ethylenedioxythiophene) (PEDOT) have been adopted as binders with electrical conductivity to further optimize the electrochemical performance of Li-S batteries. 30-33 However, these conducting polymer binders by conventional process failed to generate a uniform and conformal coverage layer on the surface of active material particles. 30, 34 The discontinuous conducting polymer layer may only provide limited conductivity enhancement since it is unable to form a consecutive conductive network in the cathode. 35 Moreover, the released polysulfides from the uncovered region of the sulfur cathode can lead to the shuttle effect and eventually battery failure.<sup>36</sup> Despite the efforts demonstrated above, strategies to instrumentally limit the sulfur shuttling effect while enhancing sulfur conversion kinetics have not been established yet for the Li-S battery. Inspired by our previous research on Ni-rich cathode modification, a fabrication method for sulfur cathode leveraging oxidative chemical vapor deposition (oCVD) is proposed in this work to address the major issues of sluggish kinetic conditions and the shuttle effect of the Li-S battery.<sup>37</sup> PEDOT was selected as the depositing polymer due to its ionic and electronic conductivity and appropriate mechanical strength under the electrochemical environment.<sup>38, 39</sup> The oCVD technique enables a highly uniform and conformal coating of PEDOT on the sulfur particles and endows multi-functionalities to the cathode. First, the continuous oCVD PEDOT (o-PEDOT) layer generates a highly efficient conductive network in all cathode regions.

Second, the o-PEDOT coating layer and the formed network works as the binder, by which the sulfur particles firmly adhere together as a unified cathode. Third, the o-PEDOT coating layer on the sulfur composite particles successfully inhibits the polysulfides shuttling within the cathode region. Consequently, these synergistic effects of o-PEDOT on sulfur cathode enabled an 84.4% sulfur utilization and capacity retention of 85% after 300 cycles (809.7 mAh g<sup>-1</sup> after 300 cycles at 0.5 C) as well as achieving >98.4% coulombic efficiency (CE). The fabricated pouch cell delivered a gravimetric energy density of 202 Wh kg<sup>-1</sup> and maintained 78% capacity after 50 cycles with a current density of 1.5 mA cm<sup>-2</sup>. The effects of o-PEDOT on the kinetic behavior and stability of the Li-S system were systematically investigated and revealed through complementary experimental and theoretical investigations. This work suggests a unique cathode fabrication strategy for Li-S batteries towards a long cycling lifespan and high energy density.

## 2. Results and Discussion

## 2.1 Fabrication and characterization of sulfur electrode

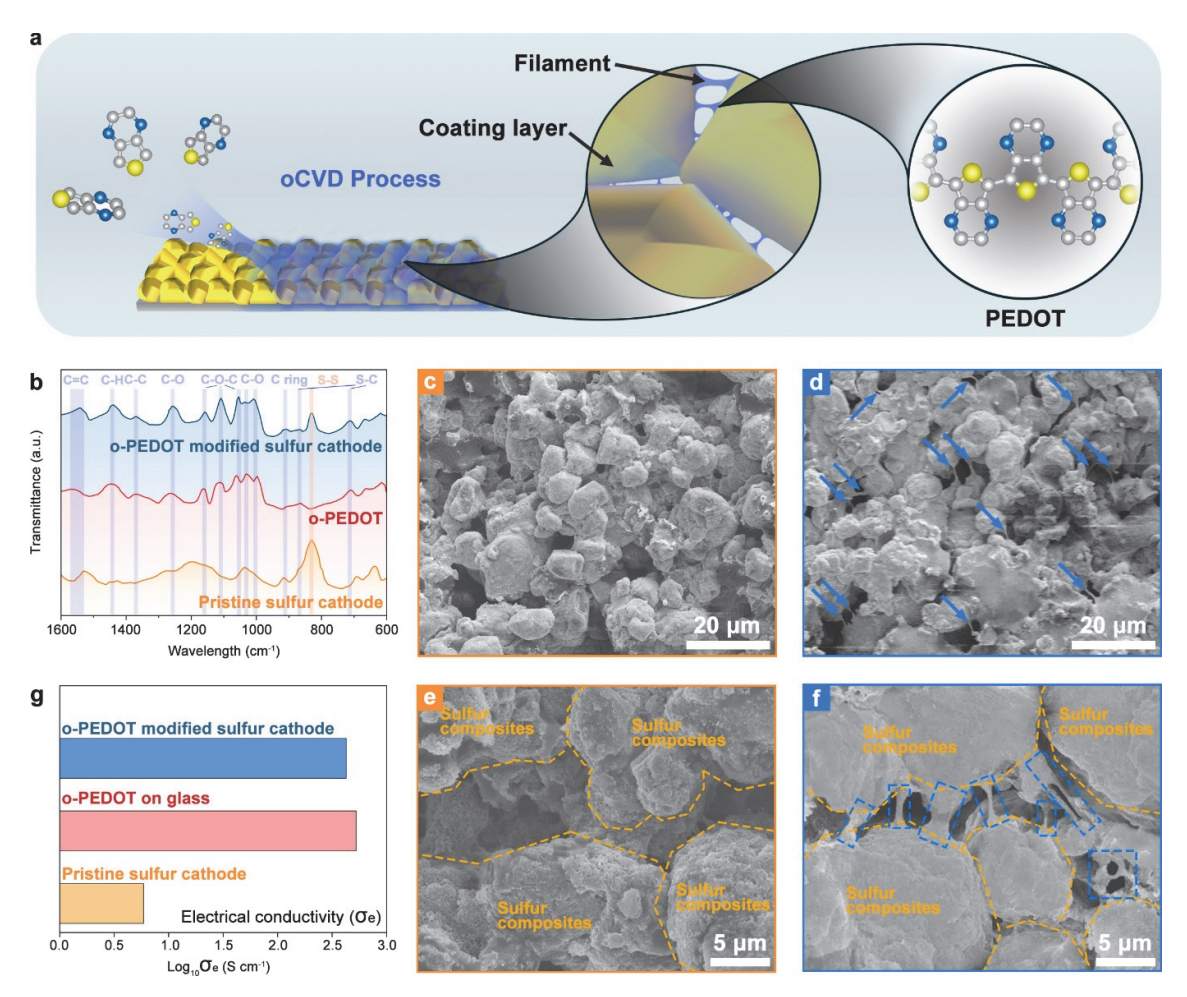


**Fig. 1.** Fabrication and characterization of the sulfur electrode. (a) Schematic of the fabrication process and features of o-PEDOT modified sulfur cathode. (b) FTIR spectra of the pristine sulfur cathode, o-PEDOT, and o-PEDOT modified sulfur cathode with detailed bond indices. (c, e) SEM images of the pristine sulfur cathode in different magnifications. (d, f) SEM images of o-PEDOT modified sulfur cathode in different magnifications. (g) Electrical conductivity of the pristine sulfur cathode, o-PEDOT on glass (reference), and o-PEDOT-modified sulfur cathode.

As schematically illustrated in Fig. 1a, a uniform mixture of sulfur composites and carbon additives was cast on Al foil, which is a semi-manufactured state without the use of binders, and then transferred into an oCVD chamber for o-PEDOT deposition. During the oCVD process, EDOT monomers were vaporized and in-situ polymerized into PEDOT through step-growth polymerization. The vapor phase coating matters were coated

on the surfaces of the sulfur composite and infiltrated into micro-voids (~5-10 µm) between the composites of the semi-manufactured electrode. The oCVD coating is typically completed within 15 mins, resulting in about 40 nm o-PEDOT films, then the manufacturing of sulfur cathode is accomplished. It should be noted that this showcased cathode manufacturing is a toxic-free approach since an n-methyl-2-pyrrolidone (NMP) solution is not necessary. The thickness of the deposited o-PEDOT layer (~ 40 nm) was measured from a reference Si wafer that was simultaneously loaded with the cathode specimen to the oCVD chamber. Fouriertransform infrared spectroscopy (FTIR) was used to compare the chemical bond information in the molecules of o-PEDOT modified sulfur cathode, pristine sulfur cathode, and o-PEDOT on Si substrate. In the FTIR spectrum obtained from an o-PEDOT-coated sulfur cathode (top of Fig. 1b), the S-S stretching peak is evidently detected at ~850 cm<sup>-1</sup>, which is concurred with the pristine sulfur cathode (bottom of Fig. 1b).<sup>40</sup> In addition, the o-PEDOT-modified sulfur cathode also exhibits characteristics peaks that agree with those of o-PEDOT deposited on Si (middle of Fig. 1b). A broad peak appeared in 1500 and 1600 cm<sup>-1</sup> corresponds to the C=C stretching of the thiophene ring of PEDOT. Other typical peaks of PEDOT caused by C-C and C-H interactions are found at ~1500-1350 cm<sup>-1</sup> in the o-PEDOT modified sulfur cathode. 41, 42 The FTIR responses of the o-PEDOT-modified cathode sustaining both characteristic bonds (i.e., o-PEDOT and sulfur cathode) verify that an o-PEDOT layer has been successfully coated on the sulfur cathode. The coating of o-PEDOT is further supported by EDS elemental mapping (Fig. S1), comparing o-PEDOT modified sulfur cathode to the pristine cathode since strong Cl signal from the modified cathode is attributed to the doping species (from FeCl<sub>3</sub> agents) in o-PEDOT.

The effect of o-PEDOT coating on the structure and surface morphology of the sulfur cathode was investigated by scanning electron microscopy (SEM) with a wide range of magnifications. In Fig. 1c and 1d, the microstructure of sulfur composites is displayed, from which the diameters of the particles are estimated

at around 10 µm for both pristine (Fig. 1c) and o-PEDOT modified (Fig. 1d) cathodes. The well-maintained porous structure in the o-PEDOT-modified cathode indicates that the architecture of the sulfur cathode was not altered during the o-PEDOT deposition process.

However, the surface morphology of the o-PEDOT modified cathode (Fig. 1f and Fig. S2b) shows a smoother surface attributed to the uniform and continuous o-PEDOT coating coated on the sulfur composite particles, compared to that of the pristine cathode (Fig. 1e and Fig. S2a). Additional microstructures are observed in SEM images of the o-PEDOT-modified cathode, where sulfur composite particles are networked (marked by blue arrows and blue rectangular in low and high magnification images respectively) in the o-PEDOT modified sulfur cathode. The o-PEDOT networks may enhance the adhesion and cohesion strength of the sulfur cathode, resulting in the higher integrity of the electrode during battery cycling. In addition, the o-PEDOT with high electrical conductivity (typically 1000-2500 S cm<sup>-1</sup>) will also be networked with carbon additives, which have been shown to synergistically enhance the electrical conductivity of the sulfur cathode. A3, A4 Detailed effects of o-PEDOT modification will be systematically presented in the comparisons of its counterparts in the later part of this study.

Four-probe measurements were conducted on o-PEDOT modified sulfur cathode to evaluate the effect of the stereo-conductive network on the sulfur cathode, pristine sulfur cathode, and as-prepared PEDOT. As indicated in Fig. 1g, the conductivity of the o-PEDOT-modified sulfur cathode is noteworthily enhanced to 427 S cm<sup>-1</sup>, which is 73 times higher than the 5.9 S cm<sup>-1</sup> of the pristine sulfur cathode. The much-enhanced conductivity of the modified cathode is attributed to the highly conductive nature of o-PEDOT (524 S cm<sup>-1</sup>) by which the electron transport in the o-PEDOT modified sulfur cathode is significantly facilitated along the formed conductive networks of the o-PEDOT sulfur cathode while the electron transport in the pristine cathode is quite limited. To obtain mechanics insight into the cathode, the tensile test and peeling test

were employed to evaluate the mechanical properties of the cathodes (P1, P2, and PE). The sulfur cathode with o-PEDOT shows higher strength in the displacement regime up to 600 µm (Fig. S3a and inset) than the other P1 and P2 cathodes. This enhanced mechanical strength of the PE cathode indicates high enough adhesion strength to accommodate the volume variation of the sulfur cathode, compared not only to the pristine P1 but also to the P2 cathode with the typical 10% PVDF binders. Moreover, the o-PEDOT sulfur cathode exhibited much higher force in the peeling test demonstrated in Fig. S3b, with fewer active materials delaminated from the sulfur cathode compared to the cathode without binder materials (P1) and even comparable (or slightly lower) with the cathode used 10 wt. % of binder materials (P2), which confirms the adhesion and cohesion strength of the o-PEDOT sulfur cathode is suitable for practical sulfur cathode applications.

# 2.2 Electrochemical kinetics and stability performance

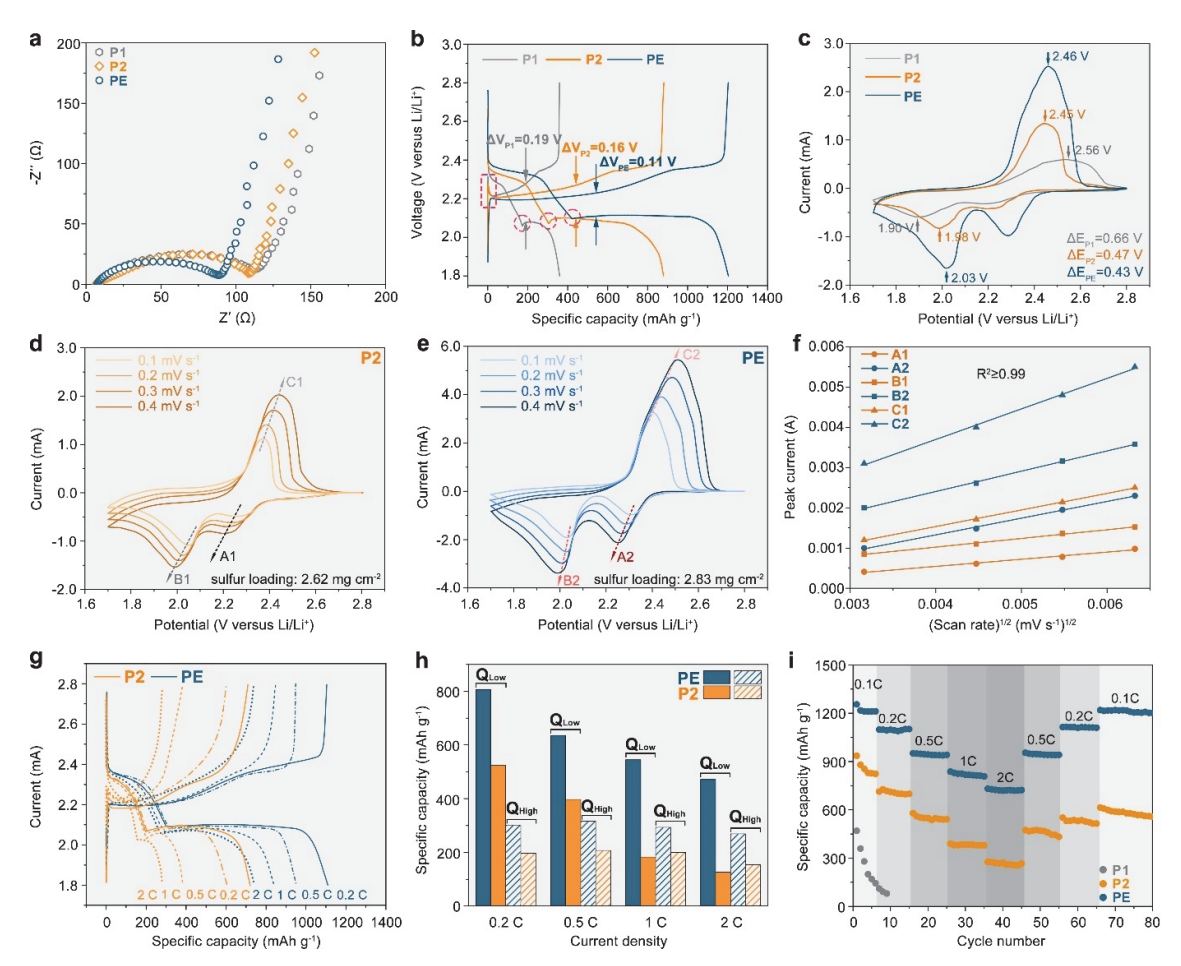


Fig. 2. Electrochemical kinetic properties of P1, P2, and PE cathodes. (a) EIS spectra of the cathodes before cycling. (b) Comparison of discharge-charge profiles of the Li-S cells with different cathodes (P1, P2, and PE) at 0.1 C rate. (c) CV plots of these cathodes at 0.1 mV s<sup>-1</sup> within a potential window of 1.7-2.8 V (versus Li/Li<sup>+</sup>). (d, e) CV profiles at different scan rates of Li-S cells with P2 and PE cathodes. (f) The linear fits (R<sup>2</sup> $\geq$ 0.99) of the CV peak currents for Li-S cells with P2 cathode (A1, B1, C1) and with PE cathode (A2, B2, C2). (g) Discharge-charge profiles of cells with P2 and PE cathodes at 0.1 C, 0.5 C, 1 C, and 2 C. (h)  $Q_{\text{High}}$  and  $Q_{\text{Low}}$  of cells with P2 and PE cathodes. (i) Rate performance of P1, P2, and PE cathodes.

To evaluate the effect of the oCVD PEDOT cathode modification on the electrochemical performance, sulfur cathodes named P1, P2, and PE were prepared. The same cathode active materials and conductive carbon were chosen for consistency to control all other factors. No PVDF binder was used in the P1 cathode while the P2 cathode was fabricated through the traditional method with the PVDF binder (~9 wt.%). The PE cathode was further manufactured by the coating of o-PEDOT on the P1 cathode. The detailed electrode

preparation procedures are available in the Experimental Section. Electrochemical impedance spectra (EIS) measurements were carried out to confirm the alternating current impedance of the two cells before cycling (Fig. 2a). The first intercept at the Z' real axis (at high frequency) corresponds to the electrolyte resistance  $(R_{\rm e})$  and the charge-transfer resistance  $(R_{\rm ct})$  is identified in the medium-low frequency range. 45, 46 It shows all cathodes yield similar  $R_e$  as indicated by the enlarged EIS plot in Fig. S4 and Table S1. However, the PE cathode displays the lowest  $R_{ct}$  value (64  $\Omega$ ) compared with the P1 (109  $\Omega$ ) and P2 (101  $\Omega$ ) cathodes, which is attributed to the enhanced electronic conductivity achieved from the conformal o-PEDOT coating. The electrochemical performance of the resulting P1, P2, and PE cathodes in Li-S cells was systematically investigated. The 2<sup>nd</sup> charge/discharge profiles of cells with these cathodes at 0.1 C are plotted in Fig. 2b. The cell with the PE cathode exhibits a lower voltage polarization ( $\Delta V_{PE} < \Delta V_{P2} < \Delta V_{P1}$ ) and delivers a capacity of 1204.1 mAh g<sup>-1</sup> at 0.1 C, considerably higher than those of other cells with P1 cathode (359.3 mAh g<sup>-1</sup>) and P2 cathode (880.7 mAh g<sup>-1</sup>). Besides, in the charge profiles of the cell with P1 and P2 cathode, distinct potential barriers are observed at the beginning of the charging process as marked in the red rectangle, which demonstrates the presence of non-conductive Li<sub>2</sub>S<sub>2</sub> and Li<sub>2</sub>S generated on the surface of the electrode as well as huge polarization.<sup>47</sup> Furthermore, the discharge plot of the P1 and P2 cathode shows a lower value of nucleation overpotential of 2.06 V and 2.07 V, respectively, compared to 2.10 V of the PE cathode as marked with red circles in Fig. 2b. This decreased overpotential of the discharge process suggests the retarded diffusion kinetics of the solid-solid reduction of Li<sub>2</sub>S<sub>2</sub> to Li<sub>2</sub>S has been relieved to a large extent in the cell with PE cathode. The PE cathode delivers a further enhanced initial capacity of 1413.1 mAh g<sup>-1</sup> at 0.1 C with a Ni-foam current collector, which demonstrates the potential applicability of suggested oCVD cathode modification to 3D structured cathodes as well as 2D planar cathodes (Fig. S5).

The electrochemical behavior of coin cells configured with P1, P2, and PE cathodes is further studied by

cyclic voltammetry (CV) measurements. The CV profiles of all cathodes (P1, P2, and PE) exhibit two major reduction peaks around 2.0 V and 2.3 V, as demonstrated in Fig. 2c. Theoretically, the peak at higher voltage corresponds to the reduction of sulfur to high-order polysulfides (Li<sub>2</sub>S<sub>n</sub>,  $4 \le n < 8$ ), and the peak at lower voltage is related to the conversion of polysulfides from higher order to lower order (Li<sub>2</sub>S<sub>2</sub> and Li<sub>2</sub>S). The main oxidation peak located at about 2.4 V is associated with the reaction of polysulfides from lower to higher order. With similar mass loading for each cathode sample, the PE cathode displays a higher magnitude of all reduction and oxidation peaks compared to the P1 and P2 cathodes, which demonstrates the enhanced sulfur conversion reaction kinetics. Moreover, the PE cathode sample exhibits the reduction peaks at a relatively higher voltage (2.03 V) as indicated by arrows in Fig. 2c, and the narrower peak potential difference  $\Delta E$  ( $\Delta E_{PE} = 0.43$  V,  $\Delta E = E_{oxidation} - E_{reduction}$ ) compared to P1 ( $\Delta E_{P1} = 0.66$  V) and P2 ( $\Delta E_{P2} = 0.47$  V), implying the electrochemical reaction has the lowest resistance in the PE cathode.

Li-S cells with the P2 and PE cathodes were constructed for the lithium-ion diffusion coefficient test. The voltammogram of the Li-S cell with the PE cathode in Fig. 2e shows more pronounced redox peaks, demonstrating higher currents and lower polarization than the cell with the P2 cathode in Fig. 2d. Upon subsequent increased scan rate from 0.1 mV s<sup>-1</sup> to 0.4 mV s<sup>-1</sup>, both cells with the P2 and PE cathodes exhibit a gradual rise in the current intensities, while PE cathode has higher current densities at each redox peak (A2, B2, and C2) in various scan rates than those (A1, B1, and C1) of P2 cathode, which may be primarily attributed to the improved lithium-ion diffusion capability at the electrode/electrolyte interface. The Randles-Sevick equation<sup>48, 49</sup> below was employed to estimate the diffusion coefficient of Li-ion, and the results are plotted in Fig. 2f:

$$I_p = 2.69 \times 10^5 n^{1.5} A D_{Li}^{0.5} C_{Li} v^{1.5}$$

Where Ip indicates the peak current, n is the number of electrons in the reaction, A is the electrode area, v is

the scanning rate, and  $C_{Li}$  is the lithium-ion concentration in the electrolyte. The lithium-ion diffusion coefficient of the PE cathode (0.62-2.23 × 10<sup>-8</sup> cm<sup>2</sup> s<sup>-1</sup>) is higher than that of the P2 cathode (0.24-0.88 × 10<sup>-8</sup> cm<sup>2</sup> s<sup>-1</sup>) as compared in Table S2. The increased Li-ion diffusion coefficient with the PE cathode verifies the elevated Li-S conversion kinetics.<sup>50</sup> In the PE cathode, the o-PEDOT works as a stereo-conductive network with carbon additives to provide more electronic conducting paths for electron transport, resulting in low  $R_{ct}$  and high  $D_{Li}$ .

Galvanostatic discharge-charge profiles of P2 and PE cathodes were obtained at current densities of 0.2 C, 0.5 C, and 1 C, respectively (Fig. 2g). The cell with PE cathode shows a smaller potential barrier at various current densities compared to that with P2 cathode, which indicates preferable reaction kinetics with faster charge and mass transportation of the cell with PE cathode. In addition, the cell with the PE cathode shows lower voltage polarization of 0.16 V at 0.5 C and 0.17 V at 1 C as detailed in Fig. S6, compared with 0.19 and 0.20 V of the P2 cathode, respectively, further indicating the superior reaction kinetic and good stability of the PE cathode achieved by the o-PEDOT multifunctional layer.

Besides, a multistep sulfur conversion reduction to Li<sub>2</sub>S upon accepting Li-ions and electrons can be identified through the plateaus at high and low voltage regions in Fig. 2b and 2g.<sup>51</sup> The generation of soluble LiPSs and liquid-liquid conversion between long-chain and short-chain LiPSs take place at the high voltage range. The low voltage range corresponds to the deposition of Li<sub>2</sub>S, which is regarded as liquid-solid conversion. The identification of these two voltage ranges is illustrated in Fig. S6.

The capacities of the high plateau ( $Q_{High}$ ) and low plateau ( $Q_{Low}$ ) of discharge profiles in Fig. 2g are used to evaluate the kinetic promotion efficiency of P2 and PE cathodes for the liquid-liquid and liquid-solid conversion processes.<sup>52, 53</sup> The cell with PE cathode exhibits the higher  $Q_{High}$  at 0.2 C (302.4 mAh g<sup>-1</sup>), 0.5 C (316.2 mAh g<sup>-1</sup>), 1 C (292.7 mAh g<sup>-1</sup>), and 2 C (269.1 mAh g<sup>-1</sup>) compared with 196.8 mAh g<sup>-1</sup>, 207.1 mAh

g<sup>-1</sup>, 199.5 mAh g<sup>-1</sup>, and 153.8 mAh g<sup>-1</sup> of P2 cathode under corresponding current densities, which supports that the generation of LiPSs and the liquid-liquid conversion between soluble LiPSs in the PE cathode has been effectively promoted in the cathode. In addition, the cell with PE cathode afforded the  $Q_{Low}$  of 807.4 mAh g<sup>-1</sup>, 636.3 mAh g<sup>-1</sup>, 545.6 mAh g<sup>-1</sup> and 472.1 mAh g<sup>-1</sup>at 0.2 C, 0.5 C, 1 C and 2 C, respectively, which is higher than 523.9 mAh g<sup>-1</sup>, 397.2 mAh g<sup>-1</sup>, 183.4 mAh g<sup>-1</sup> and 126.3 mAh g<sup>-1</sup> with the P2 cathode (Fig. 2h; Table S3). The higher capacity in  $Q_{Low}$  is due to the enhanced kinetics of charged carriers in the PE cathode on the liquid-solid conversion process.<sup>54</sup>

The rate performance of the Li-S cells is illustrated in Fig. 2i, which depends on the kinetic capability of each cathode during the electrochemical process. Among the P1 and P2 control samples, the P1 cathode exhibits the poorest rate performance, which has the lowest reversibility and is continually degraded due possibly to the absence of polymer binders. The P2 cathode demonstrates a mediocre rate capability which is better than the cathode without a polymer binder (i.e., the P1 cathode). However, the PE cathode delivers the corresponding discharge capacities of 1205.3, 1109.2, 952.9, 850.7, and 741.2 mAh g<sup>-1</sup> at 0.1 C, 0.2 C, 0.5 C,1 C, and 2 C, respectively.

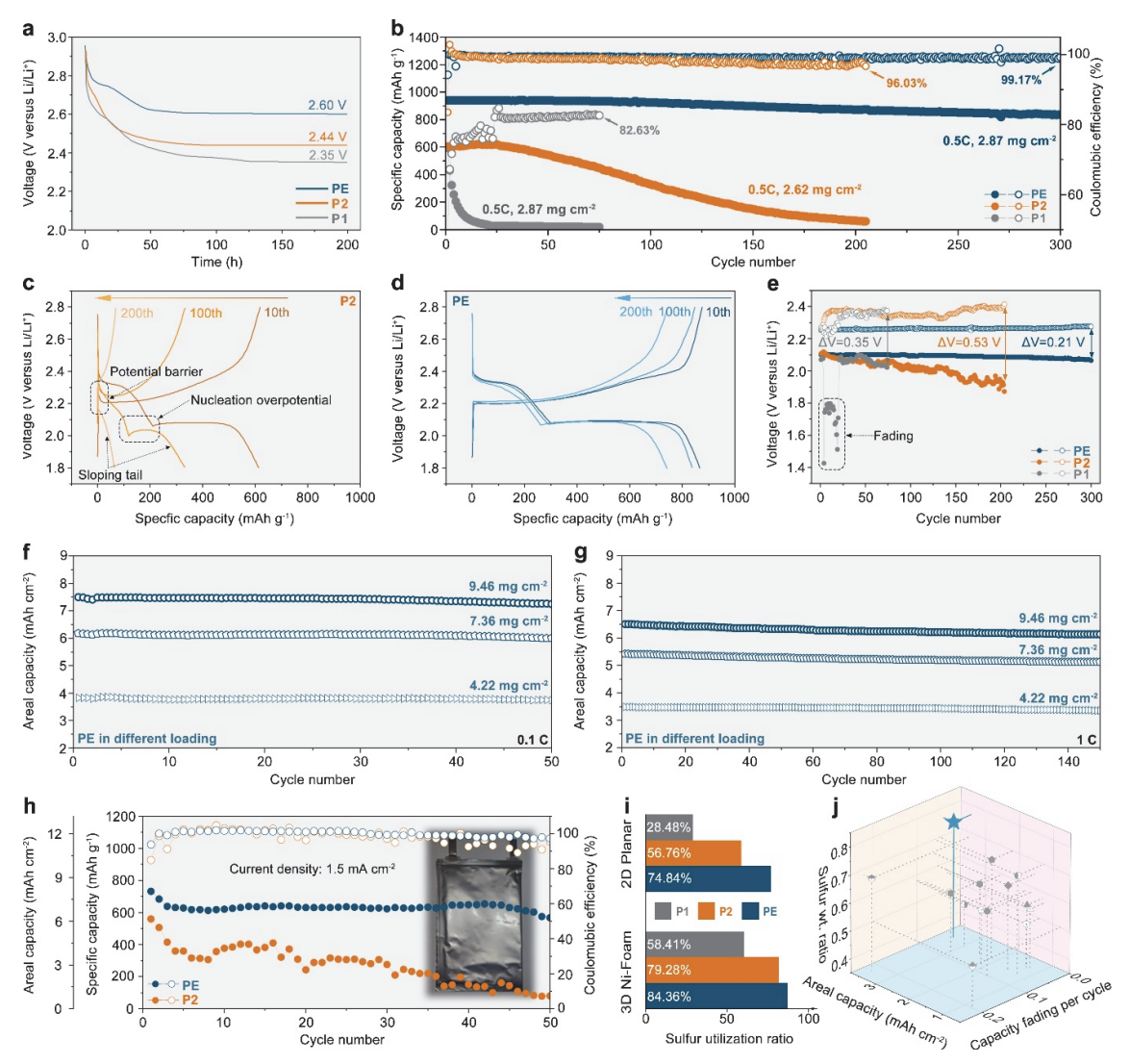


**Fig. 3.** Electrochemical stability and capacity retention of P1, P2, and PE cathodes. (a) The voltage profiles of fresh cells with P1, P2, and PE cathodes at the static placing process. (b) Long-term cycling stability of different cathodes at 0.5 C. (c, d) Discharge-charge profiles of cells with the P2 and PE cathodes at different cycles under 0.5 C. (e) Evolution of the average charge/discharge voltage (calculated by energy/capacity). (f, g) Cycle performance of Li-S coin cells of PE cathodes with various sulfur loading at 0.1 C and 1 C, respectively. (h) Cycling performance of Li-S pouch cell with the P2 and PE cathodes (the digital photograph of Li-S pouch cell as shown in the inset). (i) Sulfur utilization ratio of these cathodes with 2D and 3D dimensional cathodes at 0.1 C. (j) Comparison of the electrochemical performance of the PE cathode (i.e., this study marked as a blue star) with reported results. The related data are summarized in Table S6 in the Supporting Information.

Self-discharge behaviors were evaluated and compared to verify the effect of o-PEDOT on inhibiting sulfur species transport. Voltage changes for 200 hours were monitored from fresh cells with P1, P2, and PE

cathodes. As shown in Fig. 3a, P1, P2, and PE cathodes demonstrate voltage drops and eventually achieve 2.35 V, 2.44 V, and 2.60 V, respectively. The voltage drop within the static placement process can be ascribed to (1) the complete infiltration of the electrolyte to the conductive interface (i.e., between electrolyte and cathode); (2) the partial formation of electrode electrolyte interphases; and (3) the diffusion of LiPSs to the anode that comes from the sulfur conversion reaction.<sup>55</sup> In considering the same electrolyte amount applied in each cell and the similar sulfur loading of these cathodes, the highest voltage of PE cathode compared with P1 and P2 after 200 h can be attributed to the excellent capability of o-PEDOT for restricting the transport of LiPSs.

The long-term cycling stability of various cathodes in coin cells at 0.5 C is shown in Fig. 3b. The PE cathode offers the best cycling performance with an initial capacity of 950.9 mAh g<sup>-1</sup> and 809.7 mAh g<sup>-1</sup> after 300 cycles, exhibiting a low attenuation rate (0.04% per cycle). The P2 cathode delivers only 607.4 mAh g<sup>-1</sup> during the first discharge and decays below 50 mAh g<sup>-1</sup> after 204 cycles. The P1 cathode demonstrates sharper fading from the beginning, which is ascribed to the loss of the active materials during the charge/discharge process. It is notable that the coulombic efficiency for the PE cathode is higher than 98.4%. However, the coulombic efficiency of the P2 cathode is reduced with cycling and finally reaches 96.03% at the 204<sup>th</sup> cycle, which may be led by the "polysulfide shuttling".<sup>56, 57</sup> The coulombic efficiency is not even higher than 85% for the cell with the P1 cathode, indicating severe irreversibility attributed to the lack of binders.

The 10<sup>th</sup>, 100<sup>th</sup>, and 200<sup>th</sup> discharge-charge profiles of the cells with the P2 and PE cathodes are plotted in Fig. 3c and 3d. In the charge profiles of the cell with the P2 cathode, potential barriers, which are observed at the beginning of the charging and discharging processes, are larger than those in the PE cathode, indicating greater polarization in the P2 cell. Furthermore, the sloping tail detected at the 100<sup>th</sup> and 200<sup>th</sup> discharge plot

of the P2 cathode suggests the formation of Li<sub>2</sub>S<sub>2</sub> is dominant at this stage, rather than the solid-solid reduction of Li<sub>2</sub>S<sub>2</sub> to Li<sub>2</sub>S.<sup>58</sup> The enhanced kinetics for solid-to-solid conversion is possibly attributed to the highly efficient conductive network provided by the o-PEDOT layer, providing more charge and mass transfer sites for electrolytic species such as insoluble LiPSs.

Meanwhile, the median voltage of the PE cathode during the cycling remains consistent with only a slight variation from 2.26 to 2.27 V and 2.11 to 2.09 V for the charge and discharge process, respectively (Fig. 3e). However, both P1 and P2 cathode exhibit wider variations of the median voltage, indicating the distinguished increase in polarization and impedance of the cell during cycling. The aggressive dropping of the median voltage in the discharge process at the  $4^{th}$  cycle in the P1 cathode might be caused by active material loss. EIS measurements were conducted on P1, P2, and PE cells to investigate the impedance after cycling. Fig. S7 and Table S4 illustrate the impedance spectra of half cells with P2 and PE cathode, measured after 245 and 300 cycles, respectively. The PE cathode delivers the least resistance increase in  $R_e$ ,  $R_{sf}$ , and  $R_{ct}$  compared to P1 and P2 cathodes even after the longest cycling. It is worth noting that the exceptional long cycle stability of the PE cathode stems from the preservation of the cathode integrity and the restriction of polysulfides dissolution.

The performance of the PE cathode was further evaluated with different sulfur loading to explore the capability of o-PEDOT in a high-mass loading electrode. Fig. 3f shows the areal capacity and cycle performance with various sulfur loadings using the PE cathode. Under sulfur loading of 4.22 mg cm<sup>-2</sup>, the areal capacity of 3.82 mAh cm<sup>-2</sup> (corresponds to ~924 mAh g<sup>-1</sup> as indicated in Fig. S8) remained after 50 cycles with a very low-capacity decay, which is comparable to the typical areal capacity of the cathode in commercialized Li-ion cells (approximately 4 mAh cm<sup>-2</sup>). When the sulfur loadings are raised to 7.36 and 9.46 mg cm<sup>-2</sup>, the corresponding cells can achieve an initial areal capacity of 6.18 and 7.51 mAh cm<sup>-2</sup> with

remarkable capacity retention of 96.9% and 96.2% at 0.1 C, respectively. Cells with the PE cathode were further cycled under 1 C to continue to assess the electrochemical kinetic performance of high-loading electrodes. The PE cathode with a sulfur loading of 4.22 mg cm<sup>-2</sup> delivered an areal capacity of 3.48 mAh cm<sup>-2</sup>, which corresponds to the specific capacity of 841.6 mAh g<sup>-1</sup> as shown in Fig. S9, maintained more than 96.3% of its original capacity after 150 cycles. The cathodes with sulfur loading of 7.36 and 9.46 mg cm<sup>-2</sup> achieved initial areal capacities of 5.42 and 6.52 mAh cm<sup>-2</sup> with the capacity retention of 94.5% and 94.1% after 150 cycles. Besides, the coulombic efficiencies of PE cathodes with various sulfur loading are higher than 98.4% in both 0.1 C and 1 C circumstances as indicated in Fig. S10 and S11. The results of combined metrics of areal capacity and cycle life confirm the excellent contribution of the PE cathode to the sulfur conversion and LiPSs restriction.

Pouch cells with the PE cathode and the P2 cathode were assembled to simulate the practical application of the o-PEDOT multifunctional layer in the Li-S system (Fig. 3h and Fig. S12). The PE cathode in the pouch cell delivers an initial capacity of 732.8 mAh g<sup>-1</sup> (corresponds to 8.1 mAh cm<sup>-2</sup>) at 1.5 mA cm<sup>-2</sup> with high sulfur loading around 11 mg cm<sup>-2</sup> and a lean electrolyte condition (4.55 μL mg<sup>-1</sup>). In contrast, the P2 cathode delivers only 562.7 mAh g<sup>-1</sup> (corresponds to 6.2 mAh g<sup>-2</sup>) and a lower coulombic efficiency of 85.1% than the 93.8% of the PE cathode cell. Moreover, the still high discharge capacity of 567.1 mAh g<sup>-1</sup> (corresponds to 6.3 mAh cm<sup>-2</sup>) is achieved for the PE cathode after 50 cycles, which is much higher than the cell with the P2 cathode (81.4 mAh g<sup>-1</sup>, which corresponds to 0.89 mAh cm<sup>-2</sup>). This pouch cell with the PE cathode reaches specific energy of 202 Wh kg<sup>-1</sup> calculated from Table S5, which confirms that the PE cathode is equipped with excellent stability and has great potential in the practical application of high-energy-density Li-S cells.

Of all electrochemical testaments based on coin cells, the utilization ratio of sulfur has been counted in Fig.

3i. It should be noted that the PE cathode exhibits a higher sulfur utilization ratio in both the 2D planar structure and the 3D structure of Ni-foam (Fig. S5). The PE cathode reversibly utilized 74.84% of sulfur in the 2D planar structure, whereas much lower sulfur usage of 56.76% and 28.48% were estimated for the P2 and P1 cathodes, respectively. Remarkably, the sulfur utilization ratio of the PE cathode based on Ni-foam is 84.36% which is higher than the 2D planar cathode, which was contributed by the hollow structure, increasing the specific area and catalytic activity of the Ni-foam current collector. The sulfur utilization ratio for the P1 and P2 cathode on Ni-foam has been increased to 58.41% and 79.28% compared to those in the 2D planar structure cathode, which indicates the construction of stereoscopic structured electrodes is an effective way to enhance the sulfur utilization ratio.

Fig. 3j shows a comparison of the present results with literature results of sulfur weight ratio, capacity fade, and areal capacity. Impressively, the Li-S cell, leveraging the o-PEDOT, achieved high active material weight ratio in the cathode than those previously reported results, which is of direct relevance to the enhanced energy density of the cell. In addition, the capacity fading per cycle for the cell modified with o-PEDOT is extremely small compared with those found in the literature with a similar active materials content. Detailed comparisons are summarized in Table S6.

## 2.3 Understanding the effects of the o-PEDOT multifunction layer in the Li-S system

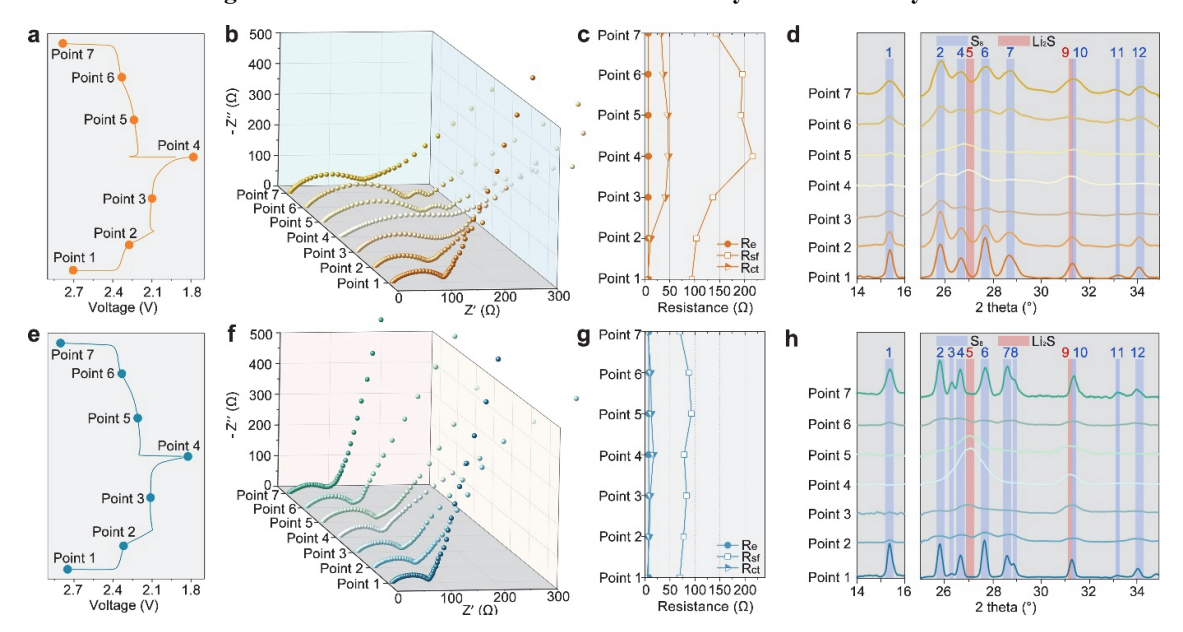


Fig. 4. The influence of o-PEDOT on activation and deposition of  $S_8$ . (a) The discharge and charge curves of the P2 cell during the  $2^{nd}$  cycle and the selected points for further investigation. (b, c) EIS spectra of all selected points in P2 cell (b) and the corresponding fitting results of  $R_e$ ,  $R_{sf}$ , and  $R_{ct}$  (c). (d) XRD results of P2 cathodes at selected points range from  $14^{\circ}-16^{\circ}$  and  $25^{\circ}-35^{\circ}$ . (e) The discharge and charge curves of the PE cell during the  $2^{nd}$  cycle and selected points for further investigation. (f, g) EIS spectra of all selected points in PE cell (f) and the corresponding fitting results of  $R_e$ ,  $R_{sf}$ , and  $R_{ct}$  (g). (h) XRD results of PE cathodes at selected points range from  $14^{\circ}-16^{\circ}$  and  $25^{\circ}-35^{\circ}$ .

To decipher the mechanism of the o-PEDOT multifunctional layer on the kinetic condition of the discharge and charge process, P2 and PE cathodes of the  $2^{nd}$  cycle at different depths of discharge (DOD) and state of charge (SOC) were characterized and analyzed. The selected DOD and SOC were marked as dots in the discharge and charge curves of both P2 and PE cathodes, as illustrated in Fig. 4a and 4e. To systematically track the change of electrochemical resistance, the EIS spectra and the XRD results were collected at multiple points of the P2 and PE cathodes. The Nyquist plots of EIS measurements show one semicircle in the high-frequency range and a short sloping tail at low frequency, which varies with different DOD and SOC for both P2 and PE cathodes. To quantify the impedance changes, all collected EIS spectra were fitted with an equivalent circuit as indicated in Fig. S13 and the value of  $R_c$ ,  $R_{sf}$ , and  $R_{ct}$  at each point is summarized for

P2 (Fig. 4c) and PE (Fig. 4g) cathodes, respectively.

In the extended EIS results (Fig. S14), the value of  $R_e$  in both P2 and PE cathodes during the full discharge and charge process is nearly constant as low as ~7  $\Omega$  during the discharge and charge process of the 2<sup>nd</sup> cycle. Yet in the  $R_{sf}$  and  $R_{ct}$  of P2 and PE cathodes, significant changes in  $R_{sf}$  and  $R_{ct}$  of both cathodes were detected. At the beginning of the discharge process in the 2<sup>nd</sup> cycle (Point 1, the end of the first cycle), the value of  $R_{sf}$  and  $R_{ct}$  in both P2 and PE cathodes is slightly lower than that before cycling (Fig. 2a), which implies the kinetic condition of the battery was promoted by the activation process within the first discharge and charge. The XRD results of P2 (Fig. 4d) and PE (Fig. 4h) cathodes at Point 1 exhibit several peaks that can be identified as sulfur (marked as the blue bar in Fig. 4d and 4h), which are generated at the end of the charging process of the first cycle. However, "peak 3" and "peak 8", which are attributed to (2 2 4) and (1 3 5) facets respectively, are only observed in the PE cathode. In addition, the full width at half maxima (FWHM) of "peak 2", "peak 4" and "peak 6" in the P2 cathode is larger than those in the PE cathode.

From Point 1 to Point 2, the solid sulfur starts reacting with Li-ions and generates soluble LiPSs (e.g., Li<sub>2</sub>S<sub>8</sub>, Li<sub>2</sub>S<sub>6</sub>, and Li<sub>2</sub>S<sub>4</sub>), dominantly consisting of Li<sub>2</sub>S<sub>8</sub> at this stage. The EIS results at this point show the higher value of  $R_{sf}$  and  $R_{ct}$  in the P2 cathode compared to the PE cathode, which implies the better kinetic condition of the PE cathode for the sulfur conversion reaction. The XRD results of the P2 cathode at Point 2 demonstrate that all peaks representing solid sulfur are still present despite the weaker intensities than those at Point 1. In contrast, "peak 1" at Point 2 is completely absent in the PE cathode (Fig. 4h), and other peaks at 2 theta of 25-35° are also nearly disappeared. The XRD results emphasize that most of the solid sulfur in the PE cathode has been consumed while the majority remains in the P2 cathode. The only difference made between the two cathodes is the o-PEDOT in the PE cathode with all others being controlled as the same. Therefore, the XRD and EIS results indicate that the o-PEDOT multifunctional layer innovatively promotes

the transformation of solid-phase sulfur to liquid-phase LiPSs in the sulfur cathode.

Within the discharge process from Point 2 to Point 3, the mid-chain and short-chain LiPSs (Li<sub>2</sub>S<sub>4</sub>, Li<sub>2</sub>S<sub>2</sub>, and Li<sub>2</sub>S) may gradually generate, among which the final solid-phase Li<sub>2</sub>S can be detected by the XRD measurement. However, due to the sluggish kinetic nature, no Li<sub>2</sub>S-related peaks were detected from the P2 cathode in Fig. 4d (i.e., no peaks at peak 9, a red bar at 2 theta = ~31.2°) while sulfur peaks are still identifiable with weak intensities. In the PE cathode, two peaks at "peak 5" and "peak 9" start being discernable at Point 3, suggesting the generation of the solid-phase Li<sub>2</sub>S from this stage. The XRD results confirm that the formation of insoluble Li<sub>2</sub>S is facilitated by the presence of o-PEDOT in the PE cathode. Furthermore, undesired  $R_{ct}$  and  $R_{sf}$  were critically increased at Point 3 of the P2 cathode, as evidenced in EIS measurements (Fig. 4b and 4c). The higher  $R_{ct}$  in the P2 cathode corresponds to the slow kinetics of the faradaic reaction, which is mainly ascribed to the formation of insoluble LiPSs14, 45. Because of the nonconductive nature of Li<sub>2</sub>S<sub>2</sub> and Li<sub>2</sub>S (i.e., insoluble LiPSs), the charge transfer only occurs at the interfaces of the electrolyte and these insoluble LIPSs. With the accumulation of Li<sub>2</sub>S and Li<sub>2</sub>S<sub>2</sub> during the discharge process, the kinetic condition of Li-ion transfer would be decreased with the reduced reaction interfaces. The increased value of  $R_{\rm sf}$  in the P2 cathode is attributed to the dissolution of soluble LiPSs, leading to weak contact between solid-phase and solid-phase inside the sulfur cathode. It should be noted that only slight changes in  $R_{ct}$  and  $R_{sf}$  of the PE cathode are observed (Fig. 4f) from Point 2 to Point 3, indicating the stable kinetic environment in the PE cell.

At the end of the discharge process in the Li-S system, which corresponds to the position of Point 4, all LiPSs are desired to be transformed to Li<sub>2</sub>S. The Point 4 XRD results of the P2 cathode, at last, exhibit two Li<sub>2</sub>S peaks ("peak 5" and "peak 9"). However, solid-phase sulfur at "peak 2" is still observed, which means a large amount of sulfur has not participated in the conversion reaction yet. On the contrary, the PE cathode

results in significant intensities of "peak 5" and "peak 9" indicating a large amount of Li<sub>2</sub>S present at Point 4, however, no sulfur peaks are visible. The  $R_{\rm ct}$  appears to be the largest in both P2 and PE cathodes at this stage, demonstrating that the reaction kinetics is slowest during the solid-solid reduction of insoluble Li<sub>2</sub>S<sub>2</sub> to Li<sub>2</sub>S. Yet the value of  $R_{ct}$  of the PE cathode at Point 4 is almost half of that of the P2 cathode, suggesting the considerably elevated kinetic conditions of the PE cathode, compared to the counterpart, for the solidsolid conversion reaction. The value of  $R_{\rm sf}$  in the P2 cathode is higher than previous points, indicating the higher concentration of the dissolved LiPSs, which means the major products at this stage are soluble LiPSs. <sup>14</sup> It should be noticed, however, that the value of  $R_{\rm sf}$  in the PE cathode is even lower than that at Point 3, which is another evidence of the generation of a large amount of solid-phase Li<sub>2</sub>S. This EIS investigation is well matched with the presented XRD results in Fig. 4h. The reduced  $R_{\rm sf}$  and hence the enhanced internal contact between the solid and solid phases favorably contributed to the kinetic performance of the PE cathode. As a result, the different reactions dominant at Point 4 between the P2 and PE cathodes further confirming the claim that the o-PEDOT in the PE cathode favors the kinetic conditions for sulfur conversion during the discharge process, compared with those of the P2 cathode. In the charging process (Point 5), the insoluble Li<sub>2</sub>S will be consumed at first and generate higher-order LiPSs. The Rct decreased in both P2 and PE cathodes compared with those at Point 4, signifying the solidliquid two-phase reaction is in progress, where insoluble LiPSs started to be oxidized to soluble LiPSs.<sup>51</sup> The faradaic reaction process has been promoted, which is likely attributed to the consumption of the solid-phase Li<sub>2</sub>S and Li<sub>2</sub>S<sub>2</sub>. The R<sub>sf</sub> of the PE cathode slightly increased compared with point 4 since the generation of soluble LiPSs weakens the contact between solid phases in the electrode, which is well supported by the XRD results of the PE cathode at Point 5. The weaker intensity of "peak 5" and "peak 9" after charging indicates the deduction of the Li<sub>2</sub>S in the PE cathode. Similarly, the amount of Li<sub>2</sub>S in the P2 cathode is

decreased at Point 5, similarly due to the weaker peaks at positions "5" and "9" in XRD results. However, a minor peak at position "1" is observed at this stage of the P2 cathode as well, which means the solid sulfur has been generated from Point 4 to Point 5 (i.e., at the beginning of the charging process). The generation of solid sulfur indicates the existence of high-order LiPSs (Li<sub>2</sub>S<sub>6</sub>, Li<sub>2</sub>S<sub>8</sub>) in the P2 cathode oxidized to solid sulfur even at the initial charging process. Meanwhile, the value of  $R_{\rm sf}$  slightly decreased from Point 4 to Point 5 of the P2 cathode, which has to be increased in theory, since the consumption of insoluble LiPSs is known to take place at this stage.<sup>51</sup> This adverse R<sub>st</sub> result further confirms the generation of solid-phase sulfur. The coexistence of high- (e.g., Li<sub>2</sub>S<sub>8</sub> and Li<sub>2</sub>S<sub>6</sub>) and low-order LiPSs (e.g., Li<sub>2</sub>S<sub>2</sub> and Li<sub>2</sub>S) is the main attribute of critically inferior kinetic conditions in the P2 cathode due to the large polarizations in the cathode. In Point 6, the presence of solid sulfur is observed in both P2 and PE cathodes although the intensities from the P2 cathode (peaks 1 and 2) are much larger than the PE cathode (only peak 2) as illustrated in Fig. 4d and 4h. The Rct at Point 6 decreased in both P2 and PE cathodes through the continuous oxidation of LiPSs driven by the charging process, which indicates the consumption of insoluble LiPSs. The value of  $R_{\rm sf}$  in the P2 cathode is nearly the same while decreasing in the PE cathode. The minor reduction in  $R_{\rm sf}$  of the PE cathode can be assigned to the improved solid-solid contact indicating the generated solid sulfur.61 The remained R<sub>sf</sub> of the P2 cathode from Point 5 to Point 6 may be contributed by the synergistic result of the formation and consumption of insoluble LiPSs. On one hand, the solid sulfur was generated from the highorder LiPSs to strengthen the solid-solid contact so that decreasing the  $R_{\rm sf}$  of the P2 cathode. On the other hand, there are still some low-order insoluble LiPSs, which will be further oxidized to soluble LiPSs. The generation of the soluble LiPSs will impair the contact between solid phases in the electrode thus increasing the  $R_{\rm sf}$ . Eventually, these two competition reaction processes lead to the unchanged  $R_{\rm sf}$  from Point 5 to Point 6.

At the end of the charging process, the value of  $R_{\rm sf}$  and  $R_{\rm ct}$  of both P2 and PE cathodes decreased compared with the values at Point 6. In addition, the value of  $R_{\rm sf}$  and  $R_{\rm ct}$  of the PE cathode at Point 7 is approximately equal to these values at Point 1. However, the overall resistance in the P2 cathode increased after the discharge and charge process (220% increase), which suggests the higher electrochemical reversibility of the PE cathode. The XRD results of both cathodes exhibit obvious peaks that are related to the sulfur, while the FWHM of all peaks in the P2 cathode is larger than that in the PE cathode, further crystalline "peak 3" and "peak 8" are only detected in the PE cathode. The higher crystallinity of the final products at Point 7 in the PE cathode suggests a higher reversibility implying favorable kinetic environments. Of note, the open PEDOT multifunctional layer was well preserved during the charge and discharge process since the characteristic peaks (highlighted in gray) at ~1550 and ~1050 cm<sup>-1</sup> of o-PEDOT from FTIR were consistent from Point 1 to Point 7 as indicated in Fig. S15, suggesting the excellent electrochemical stability of o-PEDOT multifunctional layer.

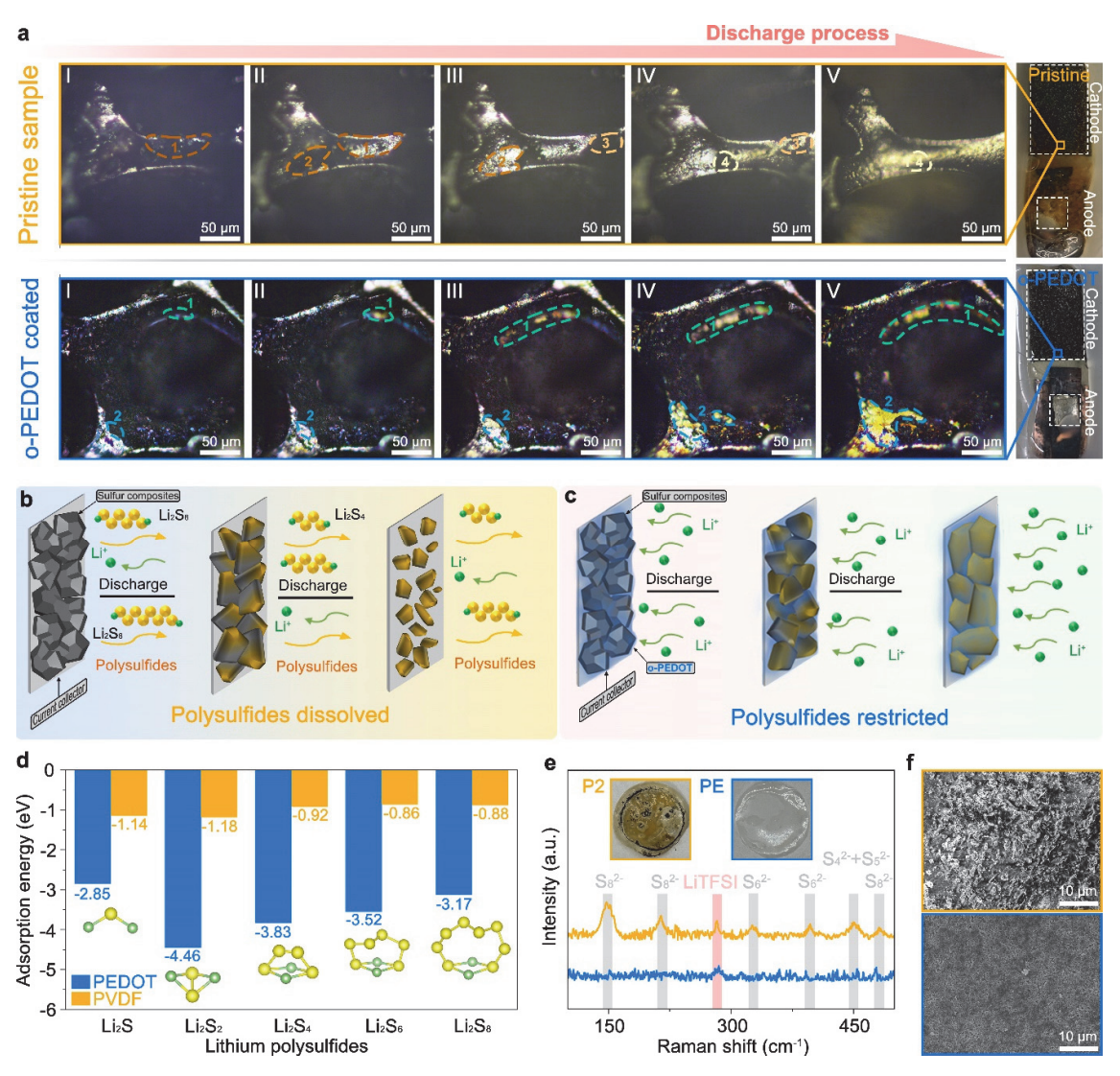


**Fig. 5.** Investigation of the effect of the o-PEDOT layer on the LiPSs restriction. (a) Optical images of sulfur cathode based on Ni-foam with and without o-PEDOT layer at discharge process and photos (on the right side) of cells after discharge. (b, c) Schematic of polysulfides dissolved in the pristine cathode and restricted in the o-PEDOT coated cathode. (d) Absorption energy of various LiPSs on PVDF and PEDOT, inset images show the molecular structure of LiPSs used in DFT calculations. (e) Raman spectra of separators from cells with the P2 and PE cathode after 100 cycles. Insets are digital images of separators. (f) SEM images of Li metal dissembled from the cell with the P2 cathode (top) and the PE cathode (bottom).

To further understand the effect of the o-PEDOT multifunctional layer on the notably enhanced battery stability and the dissolution process of sulfur composites, combinatorial studies that consist of an in-situ optical observation, ex-situ characterization, and theoretical calculations were combined to reveal the underlying mechanism for the stability and phase evolution of the sulfur cathode. The apparatus of the in-

situ optical observation system is schematically illustrated in Fig. S16a and the detailed assembling process of this observation cell was provided in Experimental Section. Ni-foam was selected as the current collector in this optical cell to visualize the evolution process of sulfur composites.

Compared to the bare Ni-foam (Fig. S17), black materials adhered to the surface of Ni-foam are clearly observed at stage I in both original and o-PEDOT coated samples (Fig. 5a). XRD results in Fig. S18 show diffraction peaks of sulfur composites and Ni further verify that sulfur composites were successfully attached to the Ni-foam current collector. Specifically, the characteristic dark blue color of PEDOT is observed in the o-PEDOT coated sample, particularly in the area without sulfur composites (black phases), which confirmed the existence of o-PEDOT. The o-PEDOT coated glass shows blue color compared with the bare glass, further implying the blue phase in the sample is the o-PEDOT layer (Fig. S19).

In stage II of the pristine sample, the sulfur composites (region marked as 1 in stage I) almost disappeared and the surface of Ni-foam (silver-like metallic color) was revealed, which means the conversion reaction of the sulfur composites was started. The generated LiPSs, which are soluble in the electrolyte, would delaminate from the current collector and dissolve into the electrolyte so that the surface of Ni-foam would be exposed.

With the discharge process continuing from stage II to stage IV, black-color in regions 2 and 3 as well as other locations of the pristine sample gradually diminished and became silver-like metallic luster (i.e., further exposure of the Ni-foam), implying more sulfur composites participated into the conversion reaction and more generated soluble LiPSs during the discharge process. However, these soluble LiPSs would be easily dissolved into the electrolyte due to the absence of the restricting medium in the original sample.

At stage V of the pristine sample, no visible phases are observed except for the Ni-foam with typical metallic luster and the overall color gradually becomes yellow during the discharge process, which is attributed to

the dissolved LiPSs in the electrolyte. Besides, the optical image of the cell based on the pristine sample shows the color of the electrolyte solvent turned yellow after discharging (Fig. 5a, right, top), which also confirms the dissolution of LiPSs.

In the o-PEDOT-coated sample, sulfur composites at regions 1 and 2 disappeared and exhibited light yellow color from stage I to II, indicating the generation of LiPSs in the o-PEDOT-coated sample. However, the generated soluble LiPSs (i.e., light-yellow-colored species) were well restricted in regions 1 and 2 without the surface exposure of Ni-foam, which suggests the dissolution of LiPSs has been limited by the o-PEDOT layer, unlike the pristine counterpart.

The area of marked regions 1 and 2, of which the initial black color changes to yellow, increased from stage II to stage IV in the PEDOT-coated sample, which denotes more active materials had been involved in the conversion reaction. And the generated discharging intermediate products (i.e., LiPSs) in the PEDOT-coated sample were preserved within these yellow-colored regions that appeared over the course of the discharge process. The formed LiPSs were confined under the o-PEDOT layer and became deeper yellow in regions 1 and 2 suggesting the higher concentration of LiPSs.

For the PEDOT-coated sample at stage V, the regions that turn into yellow especially were further increased, and the yellow color of these regions was deeper than that in previous stages, which indicates more LiPSs were concentrated beneath the o-PEDOT layer. Furthermore, the electrolyte solvent in the cell with the o-PEDOT-coated cathode was still clean and transparent after discharging as shown in Fig. 5a (right, bottom). The o-PEDOT layer demonstrates the capability of confining LiPSs to the cathode regime for both low and high-concentration LiPSs.

The sulfur dissolution process in the pristine sample is schematically demonstrated in Fig. 5b. The sulfur composites are gradually transformed to the soluble LiPSs during the discharge process, then the generated

intermediate products (Li<sub>2</sub>S<sub>8</sub>, Li<sub>2</sub>S<sub>6</sub>, and Li<sub>2</sub>S<sub>4</sub>) detach from the current collector and dissolve into the electrolyte, which will eventually lead to the "shuttle effects" and cathode capacity fading. However, in Fig. 5c describing the sulfur evolution process of the o-PEDOT-modified cell, the generated LiPSs were restricted between the current collector and the o-PEDOT layer so that the diffusion of LiPSs was only available within the cathode region.

Furthermore, calculations based on density functional theory (DFT) were performed to evaluate and compare the effects of PVDF and PEDOT on interactions with LiPSs. The adsorption configurations of each LiPSs (Li<sub>2</sub>S<sub>8</sub>, Li<sub>2</sub>S<sub>6</sub>, Li<sub>2</sub>S<sub>4</sub>, Li<sub>2</sub>S<sub>2</sub>, and Li<sub>2</sub>S) on both PVDF and PEDOT are displayed in Fig. S20. The theoretical adsorption energies between various LiPSs and PVDF as well as PEDOT are exhibited in Fig. 5d. The adsorption energies of soluble LiPSs (Li<sub>2</sub>S<sub>8</sub>, Li<sub>2</sub>S<sub>6</sub>, and Li<sub>2</sub>S<sub>4</sub>) in PEDOT were -3.17 eV, -3.52 eV, and -3.83 eV respectively, which suggests these soluble LiPSs can be strongly adsorbed by the S atoms of PEDOT. The strong Li-S interaction between Li atoms and S in o-PEDOT enables the immobilization of LiPSs.

In contrast, much lower adsorption energies for Li<sub>2</sub>S<sub>8</sub> (-0.88 eV), Li<sub>2</sub>S<sub>6</sub> (-0.86 eV), and Li<sub>2</sub>S<sub>4</sub> (-0.92 eV) are seen in the case of PVDF, indicating the weak interactions of these LiPSs with the F atoms in PVDF. The DFT calculation results indicate the PEDOT acts in chemisorbing LiPSs through the S element on the thiophane ring which largely limits the dissolution and precipitation of LiPSs into the electrolyte. Consequently, the o-PEDOT multifunctional layer can provide not only physical restriction but also chemical absorption to LiPSs hence benefitting the Li-S cells.

To experimentally confirm the LiPSs confinement capability of o-PEDOT by comparisons, the separators and Li metal anodes of the cells with P2 and PE cathodes were collected after 100 cycles. As shown in the insets of Fig. 5e, yellow species that may be caused by the accumulation of LiPSs are clearly observed in the separator of the P2 cell. However, no visible LiPSs are identified from the separator of the PE cell, which

remained clean after cycling. Additional optical images in Fig. S21 further validate the o-PEDOT capability, restricting the polysulfide transport. Fig. S21a is an optical image of Li metal disassembled from the cell with the P2 cathode, exhibiting accumulated black phases (i.e., LiPSs) on the surface. On the contrary, the Li metal taken from the PE cell (Fig. S21b) still shows the shiny metallic surface without significant accumulation of the black species.

Raman spectra of the separator in P2 and PE cells were taken from the region adjacent to the cathode as shown in Fig. 5e. The peak located at 282 cm<sup>-1</sup> that appears in both separators is contributed by LiTFSI in the electrolyte.<sup>63</sup> Several Raman peaks were generated from the separator in the P2 sample at 100 – 500 cm<sup>-1</sup>. the signals at 150 cm<sup>-1</sup>, 219 cm<sup>-1</sup> and 478 cm<sup>-1</sup> is due to S<sub>8</sub><sup>2-</sup> anions, which indicates that abundant Li<sub>2</sub>S<sub>8</sub> is released from the P2 cathode. The peaks at 326 cm<sup>-1</sup> and 392 cm<sup>-1</sup> were attributed to the released Li<sub>2</sub>S<sub>6</sub>. Moreover, the peak located at 454 cm<sup>-1</sup> represents the mixtures of mid-chain LiPSs (Li<sub>2</sub>S<sub>4</sub> and Li<sub>2</sub>S<sub>5</sub>).<sup>64, 65</sup> The coexistence of various LiPSs indicates that the serious shuttle effect occurs in the P2 cell.

Furthermore, obvious dendrite-like Li morphology is observed on the Li anode of the cell with the P2 cathode (Fig. 5f) and the corresponding EDS mapping (Fig. S22) results exhibit the high intensity of the S signals, which leads to lower Coulombic efficiency so that the performance degradation of the battery. In contrast, the Li anode paired with the PE cathode has a dense morphology with much weaker S signals on the surface, suggesting the damage of LiPSs from the cathode has been eliminated. The experimental characterization results further confirmed the o-PEDOT in the PE cathode not only helps to inhibit the LiPSs shuttle effect but also ensures the more uniform Li-ion deposition, which contributed to the extraordinary cycling stability of the cell with the PE cathode.

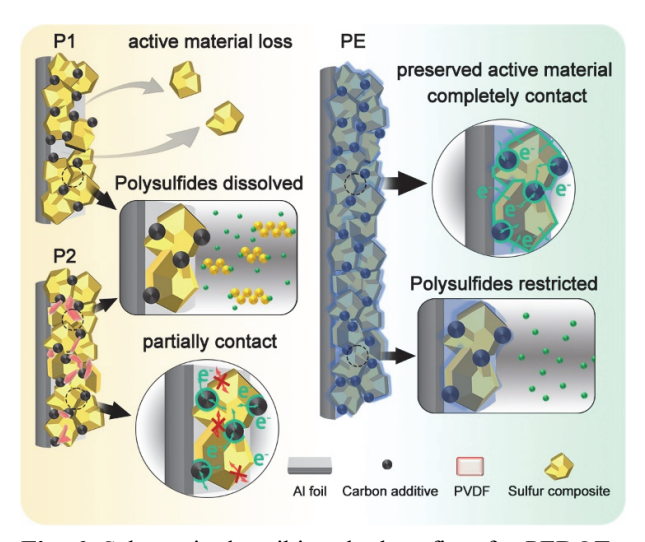


**Fig. 6.** Schematic describing the benefits of o-PEDOT on the PE cathode, compared with the P1 and P2 cathode.

#### 3. Conclusion

In summary, this study provides a facile strategy to build a stable and kinetically active sulfur cathode with high sulfur weight ratio through the oCVD technique and ultimately realize high-performance and practical Li-S batteries.

A schematic of the active material confinement and electronic path for P1, P2, and PE cathodes is proposed to summarize the different electrochemical processes (Fig. 6). For the P1 cathode, the active material can readily detach from the current collector attributed to the absence of PVDF (i.e., missing adhesion capability). In comparison, the active material in the P2 cathode can be preserved during the circulation with PVDF (approximately 9 wt%.) in the cathode. However, the electron paths only through carbon additives in the P2 cathode are limited. In addition, LiPSs are dissolved into the electrolyte in both the P1 and P2 cathodes, which leads to rapid degradation in the electrochemical performance. In contrast, the PE cathode covered by the o-PEDOT layer exhibited higher sulfur redox activity and sustained conversion reversibility, accounting for a high initial specific capacity of 850.7 mAh g<sup>-1</sup> at 1 C and utilization ratio up to 74.84% (corresponds to ~1,250 mAh g<sup>-1</sup>) at 0.1 C, and enhanced cycling retention of 85% after 300 cycles at 0.5 C with 76.5 % (in

weight ratio) sulfur in the cathode. A large-scale pouch cell using the PE cathode delivered an energy density of 202 Wh kg<sup>-1</sup> with a lean electrolyte condition.

The experimental and theoretical results further revealed that the o-PEDOT layer, enabled by oCVD, exhibits promising tri-functions in the Li-S cell by (1) providing adhesion capability in the electrode, which inhibits the loss of active materials; (2) working as highly efficient conductive networks to generate more active sites for mass and carrier transfer; and more importantly, (3) restricting the formation of LiPSs phases in the cathode by both physical separation and chemical absorption by the o-PEDOT layer.

This oCVD cathode coating approach demonstrating high sulfur weight ratio and multifunctional protection capabilities may be of significant importance to academic and industrial studies that seek enhanced performance and lifespan of the Li-S batteries.

#### 4. Experimental Section

Fabrication of the sulfur cathode: Commercial sulfur powders and carbon powders (Super P, Denka) were mixed in the mass ratio of 85:15 through a ball-milling process for 60 mins. The obtained mixture was then heated at 155 °C for 12 hours to generate sulfur composites. For the P1 and PE cathodes, the sulfur composites were mixed with carbon additives (super P and multiwall carbon nanotubes mixed in a mass ratio of 1:1) in a mass ratio of 9:1 by a magnetic stirring bar for 4 hours. Then the isopropyl alcohol was added to the mixture and mixed by the magnetic stirring process for 6 hours to obtain the homogenous slurry. A mixture of acid, which was made by the 1 wt. % HNO<sub>3</sub>, 60 wt. % H<sub>3</sub>PO<sub>4</sub>, 2 wt. % CH<sub>3</sub>COOH, and 38 wt. % DI water was adopted to etch the Al foil to enhance the surface roughness. The Al foil was merged into the etchant for 60 s at 45 °C then rinsed with DI water to remove the residual acid. For the P2 cathode, the slurry was mixed using NMP as the solvent with sulfur composites, carbon additives (super P and multiwall carbon nanotubes mixed in a mass ratio of 1:1), and PVDF in a mass ratio of 9:1:1 (approximately equal to 82:9:9) to make the relative ratio of sulfur composites to carbon additives staying consistent with that in the P1 and PE cathode. For the 2D planar electrode, all slurries were coated by a lab-scale blade on an etched Al foil and dried at room temperature in a fume hood. Several drops of isopropyl alcohol were added in front of the slurry on the Al foil to pre-wet the interface between the Al foil and slurry. The surface of the etched Al foil is rougher than unetched foil so that enables the slurry casting without binder materials. For the 3D structure electrode, 0.2 mL slurry was gradually dropped on the Ni-foam to generate P1, P2, and PE cathode and dried in a fume hood. The PE cathode will then be transferred into a custom-designed oCVD system as described in a previous report for o-PEDOT deposition.<sup>66</sup> 3,4-Ethylenedioxythiophene (EDOT, 97%, Sigma Aldrich) monomers were heated to 130 °C for vaporization and introduced into the sealed vacuum chamber. Iron chloride (FeCl<sub>3</sub>, 97%, Sigma Aldrich) was used as the oxidant and was heated to 165 °C in a crucible for sublimation. During the deposition, the flow rate of vapor-phased EDOT can be

controlled by a needle valve, and the working pressure was maintained at  $2 \times 10^{-3}$  Torr. For the cathode application, the PE cathode was attached to the substrate stage and the temperature of the substrate was kept at 100 °C. To ensure the uniform deposition of o-PEDOT on the PE cathode, the substrate was rotated at a rate of 5 rpm during deposition. After deposition, the PE cathode was rinsed with methanol to remove residual oxidants and unreacted monomers and then dried at room temperature in a fume hood. Coin cell assembly and electrochemical tests: P1, P2, and PE cathodes were cut into disks with a diameter of 12 mm and tested in CR2032 coin-type cells. Li foil and Celgard 2400 membrane were employed as anode and separator respectively. The electrolyte was constituted of 1 M Bis (trifluoromethane) sulfonamide lithium (LiTFSI) and 1,3-dioxolane (DOE)/1,2-dimethoxyethane (DME) (1:1 by volume) with 0.2 M lithium nitrate (LiNO<sub>3</sub>). The electrolyte to sulfur ratio was controlled within 7.7-10.3 μL mg<sup>-1</sup> depending on the sulfur loading. 25  $\mu$ L electrolyte was added to the cell with a sulfur loading lower than 3 mg cm<sup>-2</sup>. For the PE cathode,  $40 \mu L$ ,  $60 \mu L$ , and  $110 \mu L$  electrolytes were added for cells with various sulfur loading of 4.22 mg cm<sup>-2</sup>, 6.18 mg cm<sup>-2</sup>, and 9.46 mg cm<sup>-2</sup>, respectively. All the cell assembly processes were conducted in an argon-filled glove box. For the pouch cell, sulfur cathodes with the sulfur loading around 11 mg cm<sup>-2</sup> were cut to be 4 cm × 4 cm (cathode and Al substrate). Li foil with a thickness of 0.2 mm was cut to the same size (4 cm × 4 cm) as the anode. The Al tab was welded on the cathode and the Ni tab was welded on the Li anode through a conductive Cu tab. Celgard separator was placed between the cathode and Li anode with a certain amount of electrolyte injected into the stack. Then the package was sealed under the vacuum in an argon-filled glove box. The electrochemical performance was tested in an electrochemical workstation (VersaSTAT3 Princeton) and a battery system (LAND CT2001A) at room temperature. EIS measurements were conducted were performed under a frequency of 100 kHz-0.01 Hz with a vibration alternating current voltage of 10 mV. CV curves were obtained from 1.7-2.8 V (vs. Li<sup>+</sup>/Li) with scan rates from 0.1 mV s<sup>-1</sup> to

 $0.4 \text{ mV s}^{-1}$ . Galvanostatic discharge and charge tests were conducted at current densities ranging from 0.1 C to 2 C ( $1 \text{ C} = 1,650 \text{ mA g}^{-1}$ ) at room temperature.

Morphology and chemo-physical characterization: The thickness of o-PEDOT on Si substrates was measured by an FS-1 Ellipsometer (Film Sense), which was used as the nominal thickness for the o-PEDOT coated sulfur cathodes that were deposited concomitantly with the Si samples. The chemical and physical information of the o-PEDOT, pristine sulfur cathode, and o-PEDOT-modified sulfur cathode were performed by Fourier-transform infrared spectroscopy (FTIR, Nexus 670 ThermoNicolet Spectrometer). The electrical conductivities of o-PEDOT, pristine sulfur cathode, and o-PEDOT-modified sulfur cathode were tested by the four-probe method. A scanning electron microscopy (SEM) system (FEI Nova NanoSEM) was employed to investigate the morphology and element information of the sample. The cycled Li metal anode was rinsed with dimethyl carbonate (DMC) before SEM characterization to remove the residual lithium salt. X-ray diffraction analysis (XRD, Panalytical Empyrean Powder X-ray diffractometer) was conducted on cathodes from dissembled batteries of selected points. P2 and PE cathodes were rinsed with DMC before XRD measurements to remove the residual lithium salt. The optical images of the in-situ observation cell were recorded over time by optical microscopy (Amscope) and images of cells after the discharging process were selected and captured. Functional groups on the cycled separators were analyzed by Raman spectroscopy (WiTec Alpha 300) with 532 nm laser excitation.

Construction of in-situ observation cell: Ni-foam was cut into rectangle pieces with dimensions of 1.5 cm × 2.5 cm for pristine and o-PEDOT coated samples. 1 mL slurry made of sulfur composites and carbon additives (sulfur composites: carbon additives = 9:1 in weight ratio) was dropped on the surface of Ni-foam and dried in a fume hood. Then, a stainless-steel wire was welded on the Ni-foam electrode. The o-PEDOT coated sample was further transferred into the oCVD chamber for deposition by using the same parameters

as the PE cathode. Li metal was used as the anode and copper tape was selected as the current collector for the anode. The cell case was built by stereolithography 3D printing as shown in Fig. S16c. A microscope glass (Amscope, 50 mm × 24 mm) was covered on the cell case and sealed by a plastic welder. The cell was assembled in an argon-filled glove box.

Computational method: DFT calculations were carried out using the Vienna Ab initio Simulation Package (VASP).<sup>67, 68</sup> The projector augmented wave (PAW) pseudopotentials are utilized to describe the core and valence electrons.<sup>69</sup> The generalized gradient approximation based on the Perdew-Burke-Ernzerhof was employed to describe the electron exchange and correlation.<sup>70</sup> An energy cut-off of 450 eV and the k-point of  $1 \times 1 \times 1$  were used to indicate the Brillouin zones of molecules with and without the adsorption of lithium polysulfides. The adsorption energy ( $E_{ads}$ ) was calculated from the energy differences between adsorbed lithium polysulfide on the molecule surface ( $E_{total}$ ) and the sum of the energy of pristine molecules ( $E_{mol}$ ) and energy of lithium polysulfides ( $E_{LiPSs}$ ), which is defined as  $E_{ads} = E_{total}$ -( $E_{mol} + E_{LiPSs}$ ).

## CRediT authorship contribution statement

Yuxuan Zhang: Conceptualization, Investigation, Validation, Visualization, Writing – original draft. Han

Wook Song: Funding acquisition. Kyle R. Crompton: Writing – review & editing. Xixian Yang:

Resources. Kejie Zhao: Resources. Sunghwan Lee: Conceptualization, Methodology, Supervision, Writing – review & editing.

## **Declaration of Competing Interest**

The authors declare no competing financial interest.

# Acknowledgments

S.L. and H.W.S. acknowledge the support from the Improvement of Measurement Standards and Technology for Mechanical Metrology (Grant No. 23011043) by KRISS. S.L. also thanks a partial support from NSF, Award number CBET-2207302. S.L. and K.C. were partially supported by the Naval Surface Warfare Center, Crane Division under NCRADA-NSWCCD-17-223. The views and conclusions contained herein are those of the authors and should not be interpreted as necessarily representing the official policies or endorsements, either expressed or implied, of the Naval Surface Warfare Center, Crane Division or the U.S. Government.

## References

- (1) Goodenough, J. B.; Kim, Y. Challenges for Rechargeable Li Batteries. *Chemistry of Materials* **2010**, *22* (3), 587-603. DOI: 10.1021/cm901452z.
- (2) Bruce, P. G.; Freunberger, S. A.; Hardwick, L. J.; Tarascon, J.-M. Li-O2 and Li-S batteries with high energy storage. *Nature Materials* **2012**, *11* (1), 19-29. DOI: 10.1038/nmat3191.
- (3) Li, M.; Lu, J.; Chen, Z.; Amine, K. 30 Years of Lithium-Ion Batteries. *Advanced Materials* **2018**, *30* (33), 1800561, <a href="https://doi.org/10.1002/adma.201800561">https://doi.org/10.1002/adma.201800561</a>. DOI: <a href="https://doi.org/10.1002/adma.201800561">https://doi.org/10.1002/adma.201800561</a>. (accessed 2023/03/17).
- (4) Ji, X.; Lee, K. T.; Nazar, L. F. A highly ordered nanostructured carbon–sulphur cathode for lithium–sulphur batteries. *Nature Materials* **2009**, *8* (6), 500-506. DOI: 10.1038/nmat2460.
- (5) Ji, X.; Nazar, L. F. Advances in Li–S batteries. *Journal of Materials Chemistry* 2010, 20 (44), 9821-9826,
   10.1039/B925751A. DOI: 10.1039/B925751A.
- (6) Liu, X.; Huang, J.-Q.; Zhang, Q.; Mai, L. Nanostructured Metal Oxides and Sulfides for Lithium–Sulfur Batteries. *Advanced Materials* **2017**, *29* (20), 1601759, <a href="https://doi.org/10.1002/adma.201601759">https://doi.org/10.1002/adma.201601759</a> (accessed 2023/03/17).
- (7) He, G.; Ji, X.; Nazar, L. High "C" rate Li-S cathodes: sulfur imbibed bimodal porous carbons. *Energy & Environmental Science* **2011**, *4* (8), 2878-2883, 10.1039/C1EE01219C. DOI: 10.1039/C1EE01219C.
- (8) Zhang, S.; Xiao, W.; Zhang, Y.; Liu, K.; Zhang, X.; Zhao, J.; Wang, Z.; Zhang, P.; Shao, G. Construction of a low-defect and highly conductive 3D graphene network to enable a high sulphur content cathode for high performance Li–S/graphene batteries. *Journal of Materials Chemistry A* **2018**, *6* (45), 22555-22565, 10.1039/C8TA06869K. DOI: 10.1039/C8TA06869K.
- (9) Chen, W.-J.; Zhao, C.-X.; Li, B.-Q.; Jin, Q.; Zhang, X.-Q.; Yuan, T.-Q.; Zhang, X.; Jin, Z.; Kaskel, S.;

- Zhang, Q. A Mixed Ether Electrolyte for Lithium Metal Anode Protection in Working Lithium–Sulfur Batteries. *ENERGY & ENVIRONMENTAL MATERIALS* **2020**, *3* (2), 160-165, <a href="https://doi.org/10.1002/eem2.12073">https://doi.org/10.1002/eem2.12073</a>. DOI: <a href="https://doi.org/10.1002/eem2.12073">https://doi.org/10.1002/eem2.12073</a> (accessed 2023/03/17).
- (10) Marino, C.; Boulet, L.; Gaveau, P.; Fraisse, B.; Monconduit, L. Nanoconfined phosphorus in mesoporous carbon as an electrode for Li-ion batteries: performance and mechanism. *Journal of Materials Chemistry* **2012**, *22* (42), 22713-22720, 10.1039/C2JM34562E. DOI: 10.1039/C2JM34562E.
- (11) Marino, C.; Debenedetti, A.; Fraisse, B.; Favier, F.; Monconduit, L. Activated-phosphorus as new electrode material for Li-ion batteries. *Electrochemistry Communications* **2011**, *13* (4), 346-349. DOI: <a href="https://doi.org/10.1016/j.elecom.2011.01.021">https://doi.org/10.1016/j.elecom.2011.01.021</a>.
- (12) Chen, W.; Lei, T.; Qian, T.; Lv, W.; He, W.; Wu, C.; Liu, X.; Liu, J.; Chen, B.; Yan, C.; et al. A New Hydrophilic Binder Enabling Strongly Anchoring Polysulfides for High-Performance Sulfur Electrodes in Lithium-Sulfur Battery. *Advanced Energy Materials* 2018, 8 (12), 1702889, <a href="https://doi.org/10.1002/aenm.201702889">https://doi.org/10.1002/aenm.201702889</a>. DOI: <a href="https://doi.org/10.1002/aenm.201702889">https://doi.org/10.1002/aenm.201702889</a>. (accessed 2023/03/17).
- (13) Komaba, S.; Yabuuchi, N.; Ozeki, T.; Han, Z.-J.; Shimomura, K.; Yui, H.; Katayama, Y.; Miura, T. Comparative Study of Sodium Polyacrylate and Poly(vinylidene fluoride) as Binders for High Capacity Si–Graphite Composite Negative Electrodes in Li-Ion Batteries. *The Journal of Physical Chemistry C* **2012**, *116* (1), 1380-1389. DOI: 10.1021/jp204817h.
- (14) Fan, Q.; Jiang, J.; Zhang, S.; Zhou, T.; Pang, W. K.; Gu, Q.; Liu, H.; Guo, Z.; Wang, J. Accelerated Polysulfide Redox in Binder-Free Li2S Cathodes Promises High-Energy-Density Lithium–Sulfur Batteries.

  \*Advanced Energy Materials\*\* 2021, 11 (32), 2100957, <a href="https://doi.org/10.1002/aenm.202100957">https://doi.org/10.1002/aenm.202100957</a>. DOI: <a href="https://doi.org/10.1002/aenm.202100957">https://doi.org/10.1002/aenm.202100957</a> (accessed 2023/03/17).

- (15) Du, Z.; Chen, X.; Hu, W.; Chuang, C.; Xie, S.; Hu, A.; Yan, W.; Kong, X.; Wu, X.; Ji, H.; et al. Cobalt in Nitrogen-Doped Graphene as Single-Atom Catalyst for High-Sulfur Content Lithium–Sulfur Batteries. *Journal of the American Chemical Society* **2019**, *141* (9), 3977-3985. DOI: 10.1021/jacs.8b12973.
- (16) Chang, C.-H.; Chung, S.-H.; Manthiram, A. Effective Stabilization of a High-Loading Sulfur Cathode and a Lithium-Metal Anode in Li-S Batteries Utilizing SWCNT-Modulated Separators. *Small* **2016**, *12* (2), 174-179, <a href="https://doi.org/10.1002/smll.201502505">https://doi.org/10.1002/smll.201502505</a> (accessed 2023/03/17).
- (17) Wang, X.; Wang, Z.; Chen, L. Reduced graphene oxide film as a shuttle-inhibiting interlayer in a lithium–sulfur battery. *Journal of Power Sources* **2013**, *242*, 65-69. DOI: <a href="https://doi.org/10.1016/j.jpowsour.2013.05.063">https://doi.org/10.1016/j.jpowsour.2013.05.063</a>.
- (18) Yuan, Z.; Peng, H.-J.; Hou, T.-Z.; Huang, J.-Q.; Chen, C.-M.; Wang, D.-W.; Cheng, X.-B.; Wei, F.; Zhang, Q. Powering Lithium–Sulfur Battery Performance by Propelling Polysulfide Redox at Sulfiphilic Hosts. *Nano Letters* **2016**, *16* (1), 519-527. DOI: 10.1021/acs.nanolett.5b04166.
- (19) Jayaprakash, N.; Shen, J.; Moganty, S. S.; Corona, A.; Archer, L. A. Porous Hollow Carbon@Sulfur Composites for High-Power Lithium–Sulfur Batteries. *Angewandte Chemie International Edition* **2011**, *50* (26), 5904-5908, <a href="https://doi.org/10.1002/anie.201100637">https://doi.org/10.1002/anie.201100637</a>. DOI: <a href="https://doi.org/10.1002/anie.201100637">https://doi.org/10.1002/anie.201100637</a> (accessed 2023/03/17).
- (20) Chung, S.-H.; Manthiram, A. A Polyethylene Glycol-Supported Microporous Carbon Coating as a Polysulfide Trap for Utilizing Pure Sulfur Cathodes in Lithium–Sulfur Batteries. *Advanced Materials* **2014**, 26 (43), 7352-7357, <a href="https://doi.org/10.1002/adma.201402893">https://doi.org/10.1002/adma.201402893</a> (accessed 2023/03/17).
- (21) Liu, D.; Zhang, C.; Zhou, G.; Lv, W.; Ling, G.; Zhi, L.; Yang, Q.-H. Catalytic Effects in Lithium-Sulfur

- Batteries: Promoted Sulfur Transformation and Reduced Shuttle Effect. *Advanced Science* **2018**, *5* (1), 1700270, <a href="https://doi.org/10.1002/advs.201700270">https://doi.org/10.1002/advs.201700270</a>. DOI: <a href="https://doi.org/10.1002/advs.201700270">https://doi.org/10.1002/advs.201700270</a> (accessed 2023/03/17).
- (22) Xie, J.; Li, B.-Q.; Peng, H.-J.; Song, Y.-W.; Zhao, M.; Chen, X.; Zhang, Q.; Huang, J.-Q. Implanting Atomic Cobalt within Mesoporous Carbon toward Highly Stable Lithium–Sulfur Batteries. *Advanced Materials* 2019, 31 (43), 1903813, <a href="https://doi.org/10.1002/adma.201903813">https://doi.org/10.1002/adma.201903813</a>. DOI: <a href="https://doi.org/10.1002/adma.201903813">https://doi.org/10.1002/adma.201903813</a> (accessed 2023/03/17).
- (23) Liang, X.; Hart, C.; Pang, Q.; Garsuch, A.; Weiss, T.; Nazar, L. F. A highly efficient polysulfide mediator for lithium–sulfur batteries. *Nature Communications* **2015**, *6* (1), 5682. DOI: 10.1038/ncomms6682.
- (24) Chung, S.-H.; Luo, L.; Manthiram, A. TiS2–Polysulfide Hybrid Cathode with High Sulfur Loading and Low Electrolyte Consumption for Lithium–Sulfur Batteries. *ACS Energy Letters* **2018**, *3* (3), 568-573. DOI: 10.1021/acsenergylett.7b01321.
- (25) Sun, Z.; Zhang, J.; Yin, L.; Hu, G.; Fang, R.; Cheng, H.-M.; Li, F. Conductive porous vanadium nitride/graphene composite as chemical anchor of polysulfides for lithium-sulfur batteries. *Nature Communications* **2017**, *8* (1), 14627. DOI: 10.1038/ncomms14627.
- (26) Zhou, F.; Li, Z.; Luo, X.; Wu, T.; Jiang, B.; Lu, L.-L.; Yao, H.-B.; Antonietti, M.; Yu, S.-H. Low Cost Metal Carbide Nanocrystals as Binding and Electrocatalytic Sites for High Performance Li–S Batteries. *Nano Letters* **2018**, *18* (2), 1035-1043. DOI: 10.1021/acs.nanolett.7b04505.
- (27) Yuan, H.; Chen, X.; Zhou, G.; Zhang, W.; Luo, J.; Huang, H.; Gan, Y.; Liang, C.; Xia, Y.; Zhang, J.; et al. Efficient Activation of Li2S by Transition Metal Phosphides Nanoparticles for Highly Stable Lithium–Sulfur Batteries. *ACS Energy Letters* **2017**, *2* (7), 1711-1719. DOI: 10.1021/acsenergylett.7b00465.
- (28) Chen, Y.; Wang, T.; Tian, H.; Su, D.; Zhang, Q.; Wang, G. Advances in Lithium-Sulfur Batteries: From

- Academic Research to Commercial Viability. *Advanced Materials* **2021**, *33* (29), 2003666, <a href="https://doi.org/10.1002/adma.202003666">https://doi.org/10.1002/adma.202003666</a>. DOI: <a href="https://doi.org/10.1002/adma.202003666">https://doi.org/10.1002/adma.202003666</a> (accessed 2023/03/20).
- (29) Li, Y.; Guo, S. Material design and structure optimization for rechargeable lithium-sulfur batteries.

  Matter 2021, 4 (4), 1142-1188. DOI: https://doi.org/10.1016/j.matt.2021.01.012.
- (30) Milroy, C.; Manthiram, A. An Elastic, Conductive, Electroactive Nanocomposite Binder for Flexible Sulfur Cathodes in Lithium–Sulfur Batteries. *Advanced Materials* **2016**, *28* (44), 9744-9751, <a href="https://doi.org/10.1002/adma.201601665">https://doi.org/10.1002/adma.201601665</a> (accessed 2023/03/17).
- (31) Rao, M.; Song, X.; Liao, H.; Cairns, E. J. Carbon nanofiber–sulfur composite cathode materials with different binders for secondary Li/S cells. *Electrochimica Acta* **2012**, *65*, 228-233. DOI: https://doi.org/10.1016/j.electacta.2012.01.051.
- (32) Pan, J.; Xu, G.; Ding, B.; Chang, Z.; Wang, A.; Dou, H.; Zhang, X. PAA/PEDOT:PSS as a multifunctional, water-soluble binder to improve the capacity and stability of lithium–sulfur batteries. *RSC Advances* **2016**, *6* (47), 40650-40655, 10.1039/C6RA04230A. DOI: 10.1039/C6RA04230A.
- (33) Yan, L.; Gao, X.; Thomas, J. P.; Ngai, J.; Altounian, H.; Leung, K. T.; Meng, Y.; Li, Y. Ionically cross-linked PEDOT:PSS as a multi-functional conductive binder for high-performance lithium–sulfur batteries. *Sustainable Energy & Fuels* **2018**, *2* (7), 1574-1581, 10.1039/C8SE00167G. DOI: 10.1039/C8SE00167G.

  (34) Liu, J.; Li, R.; Chen, T.; Wan, W.; Wei, J.; Dai, C. Synergistic Effect between Poly(3,4-ethylenedioxythiophene)-poly(styrene sulfonate) Coated Sulfur Nano-Composites and Poly(vinylidene difluoride) on Lithium-Sulfur Battery. *Journal of The Electrochemical Society* **2018**, *165* (3), A557. DOI: 10.1149/2.0551803jes.

- (35) Yuan, H.; Huang, J.-Q.; Peng, H.-J.; Titirici, M.-M.; Xiang, R.; Chen, R.; Liu, Q.; Zhang, Q. A Review of Functional Binders in Lithium–Sulfur Batteries. *Advanced Energy Materials* **2018**, *8* (31), 1802107, <a href="https://doi.org/10.1002/aenm.201802107">https://doi.org/10.1002/aenm.201802107</a>. DOI: <a href="https://doi.org/10.1002/aenm.201802107">https://doi.org/10.1002/aenm.201802107</a> (accessed 2023/03/17).
- (36) Ai, G.; Dai, Y.; Ye, Y.; Mao, W.; Wang, Z.; Zhao, H.; Chen, Y.; Zhu, J.; Fu, Y.; Battaglia, V.; et al. Investigation of surface effects through the application of the functional binders in lithium sulfur batteries.

  Nano Energy 2015, 16, 28-37. DOI: <a href="https://doi.org/10.1016/j.nanoen.2015.05.036">https://doi.org/10.1016/j.nanoen.2015.05.036</a>.
- (37) Zhang, Y.; Kim, C. S.; Song, H. W.; Chang, S.-J.; Kim, H.; Park, J.; Hu, S.; Zhao, K.; Lee, S. Ultrahigh active material content and highly stable Ni-rich cathode leveraged by oxidative chemical vapor deposition.

  Energy Storage Materials 2022, 48, 1-11. DOI: <a href="https://doi.org/10.1016/j.ensm.2022.03.001">https://doi.org/10.1016/j.ensm.2022.03.001</a>.
- (38) Zhan, L.; Song, Z.; Zhang, J.; Tang, J.; Zhan, H.; Zhou, Y.; Zhan, C. PEDOT: Cathode active material with high specific capacity in novel electrolyte system. *Electrochimica Acta* **2008**, *53* (28), 8319-8323. DOI: <a href="https://doi.org/10.1016/j.electacta.2008.06.053">https://doi.org/10.1016/j.electacta.2008.06.053</a>.
- (39) Yang, Y.; Yu, G.; Cha, J. J.; Wu, H.; Vosgueritchian, M.; Yao, Y.; Bao, Z.; Cui, Y. Improving the Performance of Lithium–Sulfur Batteries by Conductive Polymer Coating. *ACS Nano* **2011**, *5* (11), 9187-9193. DOI: 10.1021/nn203436j.
- (40) Lee, J.; Choi, W. Surface Modification of Sulfur Cathodes with PEDOT:PSS Conducting Polymer in Lithium-Sulfur Batteries. *Journal of The Electrochemical Society* **2015**, *162* (6), A935. DOI: 10.1149/2.0651506jes.
- (41) Clevenger, M.; Kim, H.; Song, H. W.; No, K.; Lee, S. Binder-free printed PEDOT wearable sensors on everyday fabrics using oxidative chemical vapor deposition. *Science Advances* 7 (42), eabj8958. DOI: 10.1126/sciadv.abj8958 (accessed 2023/03/17).

- (42) Wang, X.; Zhang, X.; Sun, L.; Lee, D.; Lee, S.; Wang, M.; Zhao, J.; Shao-Horn, Y.; Dincă, M.; Palacios, T.; et al. High electrical conductivity and carrier mobility in oCVD PEDOT thin films by engineered crystallization and acid treatment. *Science Advances* 4 (9), eaat5780. DOI: 10.1126/sciadv.aat5780 (accessed 2023/03/17).
- (43) Lee, S.; Paine, D. C.; Gleason, K. K. Heavily Doped poly(3,4-ethylenedioxythiophene) Thin Films with High Carrier Mobility Deposited Using Oxidative CVD: Conductivity Stability and Carrier Transport.

  \*Advanced Functional Materials 2014, 24 (45), 7187-7196, <a href="https://doi.org/10.1002/adfm.201401282">https://doi.org/10.1002/adfm.201401282</a> (accessed 2023/03/17).
- (44) Drewelow, G.; Wook Song, H.; Jiang, Z.-T.; Lee, S. Factors controlling conductivity of PEDOT deposited using oxidative chemical vapor deposition. *Applied Surface Science* **2020**, *501*, 144105. DOI: https://doi.org/10.1016/j.apsusc.2019.144105.
- (45) Zhang, S. S.; Xu, K.; Jow, T. R. Electrochemical impedance study on the low temperature of Li-ion batteries. *Electrochimica Acta* **2004**, 49 (7), 1057-1061. DOI: https://doi.org/10.1016/j.electacta.2003.10.016.
- (46) Zhang, S. S.; Xu, K.; Jow, T. R. The low temperature performance of Li-ion batteries. *Journal of Power Sources* **2003**, *115* (1), 137-140. DOI: <a href="https://doi.org/10.1016/S0378-7753(02)00618-3">https://doi.org/10.1016/S0378-7753(02)00618-3</a>.
- (47) Lu, J.; Wang, Z.; Guo, Y.; Jin, Z.; Cao, G.; Qiu, J.; Lian, F.; Wang, A.; Wang, W. Ultrathin nanosheets of FeOOH with oxygen vacancies as efficient polysulfide electrocatalyst for advanced lithium–sulfur batteries. *Energy Storage Materials* **2022**, *47*, 561-568. DOI: <a href="https://doi.org/10.1016/j.ensm.2022.02.008">https://doi.org/10.1016/j.ensm.2022.02.008</a>. (48) Huang, J.-Q.; Zhuang, T.-Z.; Zhang, Q.; Peng, H.-J.; Chen, C.-M.; Wei, F. Permselective Graphene Oxide Membrane for Highly Stable and Anti-Self-Discharge Lithium–Sulfur Batteries. *ACS Nano* **2015**, *9*

(3), 3002-3011. DOI: 10.1021/nn507178a.

- (49) Das, S. R.; Majumder, S. B.; Katiyar, R. S. Kinetic analysis of the Li+ ion intercalation behavior of solution derived nano-crystalline lithium manganate thin films. *Journal of Power Sources* **2005**, *139* (1), 261-268. DOI: <a href="https://doi.org/10.1016/j.jpowsour.2004.06.056">https://doi.org/10.1016/j.jpowsour.2004.06.056</a>.
- (50) Wang, J.; Lin, F.; Jia, H.; Yang, J.; Monroe, C. W.; NuLi, Y. Towards a Safe Lithium–Sulfur Battery with a Flame-Inhibiting Electrolyte and a Sulfur-Based Composite Cathode. *Angewandte Chemie International Edition* **2014**, *53* (38), 10099-10104, <a href="https://doi.org/10.1002/anie.201405157">https://doi.org/10.1002/anie.201405157</a> (accessed 2023/03/17).
- (51) Conder, J.; Bouchet, R.; Trabesinger, S.; Marino, C.; Gubler, L.; Villevieille, C. Direct observation of lithium polysulfides in lithium–sulfur batteries using operando X-ray diffraction. *Nature Energy* **2017**, *2* (6), 17069. DOI: 10.1038/nenergy.2017.69.
- (52) Pan, Z.-Z.; Lv, W.; He, Y.-B.; Zhao, Y.; Zhou, G.; Dong, L.; Niu, S.; Zhang, C.; Lyu, R.; Wang, C.; et al. A Nacre-Like Carbon Nanotube Sheet for High Performance Li-Polysulfide Batteries with High Sulfur Loading. *Advanced Science* **2018**, *5* (6), 1800384, <a href="https://doi.org/10.1002/advs.201800384">https://doi.org/10.1002/advs.201800384</a>. DOI: <a href="https://doi.org/10.1002/advs.201800384">https://doi.org/10.1002/advs.201800384</a> (accessed 2023/03/17).
- (53) Huang, J.-Q.; Zhang, Q.; Wei, F. Multi-functional separator/interlayer system for high-stable lithium-sulfur batteries: Progress and prospects. *Energy Storage Materials* **2015**, *1*, 127-145. DOI: <a href="https://doi.org/10.1016/j.ensm.2015.09.008">https://doi.org/10.1016/j.ensm.2015.09.008</a>.
- (54) Zhao, M.; Li, X.-Y.; Chen, X.; Li, B.-Q.; Kaskel, S.; Zhang, Q.; Huang, J.-Q. Promoting the sulfur redox kinetics by mixed organodiselenides in high-energy-density lithium–sulfur batteries. *eScience* **2021**, *I* (1), 44-52. DOI: <a href="https://doi.org/10.1016/j.esci.2021.08.001">https://doi.org/10.1016/j.esci.2021.08.001</a>.
- (55) Hou, R.; Zhang, S.; Zhang, Y.; Li, N.; Wang, S.; Ding, B.; Shao, G.; Zhang, P. A "Three-Region" Configuration for Enhanced Electrochemical Kinetics and High-Areal Capacity Lithium-Sulfur Batteries.

- Advanced Functional Materials **2022**, 32 (19), 2200302, <a href="https://doi.org/10.1002/adfm.202200302">https://doi.org/10.1002/adfm.202200302</a>. DOI: <a href="https://doi.org/10.1002/adfm.202200302">https://doi.org/10.1002/adfm.202200302</a> (accessed 2023/03/17).
- (56) Li, Z.; Sami, I.; Yang, J.; Li, J.; Kumar, R. V.; Chhowalla, M. Lithiated metallic molybdenum disulfide nanosheets for high-performance lithium–sulfur batteries. *Nature Energy* **2023**, *8* (1), 84-93. DOI: 10.1038/s41560-022-01175-7.
- (57) Tikekar, M. D.; Choudhury, S.; Tu, Z.; Archer, L. A. Design principles for electrolytes and interfaces for stable lithium-metal batteries. *Nature Energy* **2016**, *I* (9), 16114. DOI: 10.1038/nenergy.2016.114.
- (58) Cho, C.-S.; Chang, J.-Y.; Li, C.-C. Highly symmetric gigaporous carbon microsphere as conductive host for sulfur to achieve high areal capacity for lithium–sulfur batteries. *Journal of Power Sources* **2020**, *451*, 227818. DOI: <a href="https://doi.org/10.1016/j.jpowsour.2020.227818">https://doi.org/10.1016/j.jpowsour.2020.227818</a>.
- (59) Zhou, G.; Yang, A.; Gao, G.; Yu, X.; Xu, J.; Liu, C.; Ye, Y.; Pei, A.; Wu, Y.; Peng, Y.; et al. Supercooled liquid sulfur maintained in three-dimensional current collector for high-performance Li-S batteries. *Science Advances* 6 (21), eaay5098. DOI: 10.1126/sciadv.aay5098 (accessed 2023/03/20).
- (60) Lei, J.; Liu, T.; Chen, J.; Zheng, M.; Zhang, Q.; Mao, B.; Dong, Q. Exploring and Understanding the Roles of Li2Sn and the Strategies to beyond Present Li-S Batteries. *Chem* **2020**, *6* (10), 2533-2557. DOI: https://doi.org/10.1016/j.chempr.2020.06.032.
- (61) Yao, Y.; Wang, S.; Jia, X.; Yang, J.; Li, Y.; Liao, J.; Song, H. Freestanding sandwich-like hierarchically TiS2–TiO2/Mxene bi-functional interlayer for stable Li–S batteries. *Carbon* **2022**, *188*, 533-542. DOI: <a href="https://doi.org/10.1016/j.carbon.2021.12.036">https://doi.org/10.1016/j.carbon.2021.12.036</a>.
- (62) Xu, R.; Lu, J.; Amine, K. Progress in Mechanistic Understanding and Characterization Techniques of Li-S Batteries. *Advanced Energy Materials* **2015**, *5* (16), 1500408, <a href="https://doi.org/10.1002/aenm.201500408">https://doi.org/10.1002/aenm.201500408</a> (accessed 2023/03/17).

- (63) Rey, I.; Lassègues, J. C.; Grondin, J.; Servant, L. Infrared and Raman study of the PEO-LiTFSI polymer electrolyte. *Electrochimica Acta* **1998**, *43* (10), 1505-1510. DOI: <a href="https://doi.org/10.1016/S0013-4686(97)10092-5">https://doi.org/10.1016/S0013-4686(97)10092-5</a>.
- (64) Lei, T.; Chen, W.; Lv, W.; Huang, J.; Zhu, J.; Chu, J.; Yan, C.; Wu, C.; Yan, Y.; He, W.; et al. Inhibiting Polysulfide Shuttling with a Graphene Composite Separator for Highly Robust Lithium-Sulfur Batteries.

  \*Joule 2018, 2 (10), 2091-2104. DOI: https://doi.org/10.1016/j.joule.2018.07.022.
- (65) Hagen, M.; Schiffels, P.; Hammer, M.; Dörfler, S.; Tübke, J.; Hoffmann, M. J.; Althues, H.; Kaskel, S. In-Situ Raman Investigation of Polysulfide Formation in Li-S Cells. *Journal of The Electrochemical Society* **2013**, *160* (8), A1205. DOI: 10.1149/2.045308jes.
- (66) Im, S. G.; Gleason, K. K. Systematic Control of the Electrical Conductivity of Poly(3,4-ethylenedioxythiophene) via Oxidative Chemical Vapor Deposition. *Macromolecules* **2007**, *40* (18), 6552-6556. DOI: 10.1021/ma0628477.
- (67) Kresse, G.; Furthmüller, J. Efficiency of ab-initio total energy calculations for metals and semiconductors using a plane-wave basis set. *Computational Materials Science* **1996**, *6* (1), 15-50. DOI: <a href="https://doi.org/10.1016/0927-0256(96)00008-0">https://doi.org/10.1016/0927-0256(96)00008-0</a>.
- (68) Kresse, G.; Furthmüller, J. Efficient iterative schemes for ab initio total-energy calculations using a plane-wave basis set. *Physical Review B* **1996**, *54* (16), 11169-11186. DOI: 10.1103/PhysRevB.54.11169.
- (69) Kresse, G.; Joubert, D. From ultrasoft pseudopotentials to the projector augmented-wave method. *Physical Review B* **1999**, *59* (3), 1758-1775. DOI: 10.1103/PhysRevB.59.1758.
- (70) Perdew, J. P.; Burke, K.; Ernzerhof, M. Generalized Gradient Approximation Made Simple. *Physical Review Letters* **1996**, 77 (18), 3865-3868. DOI: 10.1103/PhysRevLett.77.3865.